Physica D 253 (2013) 23–39

Contents lists available at SciVerse ScienceDirect

Physica D

journal homepage: www.elsevier.com/locate/physd

# On localised hotspots of an urban crime model

David J.B. Lloyd *, Hayley O'Farrell

*Department of Mathematics, University of Surrey, Guildford, GU2 7XH, UK*

## HIGHLIGHTS

- Novel localised patterns are found in an urban crime model.
- Localised patterns are followed from Turing instability to the singular limit.
- The singular limit and Turing instability are analysed using asymptotics.
- Existence of radial spots in the urban crime model is proved.
- Localised 2D patterns are numerically investigated.

## ARTICLE INFO

*Article history:*
Received 16 April 2012
Received in revised form
23 January 2013
Accepted 13 February 2013
Available online 19 February 2013
Communicated by J. Dawes

*Keywords:*
Homoclinic snaking
Singular perturbation analysis
Pattern formation

## ABSTRACT

We investigate stationary, spatially localised crime hotspots on the real line and the plane of an urban crime model of Short et al. [M. Short, M. DÓrsogna, A statistical model of criminal behavior, Mathematical Models and Methods in Applied Sciences 18 (2008) 1249–1267]. Extending the weakly nonlinear analysis of Short et al., we show in one-dimension that localised hotspots should bifurcate off the background spatially homogeneous state at a Turing instability provided the bifurcation is subcritical. Using path-following techniques, we continue these hotspots and show that the bifurcating pulses can undergo the process of homoclinic snaking near the singular limit. We analyse the singular limit to explain the existence of spike solutions and compare the analytical results with the numerical computations. In two-dimensions, we show that localised radial spots should also bifurcate off the spatially homogeneous background state. Localised planar hexagon fronts and hexagon patches are found and depending on the proximity to the singular limit these solutions either undergo homoclinic snaking or act like "multi-spot" solutions. Finally, we discuss applications of these localised patterns in the urban crime context and the full agent-based model.



## 1. Introduction

The publication of serious crime data (such as time and street location) for large cities has shown that criminal activity tends to be spatially localised into regions called crime 'hotspots': regions where high criminal activity is surrounded by low criminal activity [1,2]. One possible explanation for these hotspots is the 'near-repeat' victimisation and broken windows effect where a region (street/house etc.) has had one criminal event then there is a high probability of a subsequent criminal event to occur [3,4]. Other possible theories proposed to explain crime hotspots include the effect of police [5] and global social influence [6].

Based on the broken-window effect and 'near-repeat' victimisation theory, Short et al. [4] postulated a stochastic agent-based model for criminal activity (say burglary) on a square lattice where the lattice sites are possible locations for criminal attacks e.g. houses or neighbourhoods. Simulations of the agent-based model showed that for certain parameter values crime hotspots were observed. In order to analyse the model, a mean-field PDE was derived from the agent-based model in the limit of small time and space steps. The PDE describes the attractiveness (to burgle) field $A$ and a density of criminals field $\rho$. In non-dimensional variables, the PDE is given by [4]

$$\frac{\partial A}{\partial t} = \eta^2\nabla^2 A - A + A^0 + \rho A, \tag{1.1a}$$

$$\frac{\partial \rho}{\partial t} = \nabla\cdot\left(\nabla\rho - \frac{2\rho}{A}\nabla A\right) - \rho A + \bar{A} - A^0, \tag{1.1b}$$

where $A^0$ is the non-dimensional baseline attractiveness value, $\bar{A}$ is a constant and $\eta$ describes the rate at which the attractiveness at one site spreads to near-by sites. From such a model, one now wishes to find the large-scale distribution of the criminal activity on a two-dimensional domain and hence predict where crime hotspots are likely to occur.

In Short et al. [4], they showed numerically that (1.1) possessed spatially doubly-periodic crime patterns. Crucial to the existence

* Corresponding author.
*E-mail address:* d.j.lloyd@surrey.ac.uk (D.J.B. Lloyd).

0167-2789/$ – see front matter © 2013 Elsevier B.V. All rights reserved.
http://dx.doi.org/10.1016/j.physd.2013.02.005

of stationary spatially periodic crime hotspots is the presence of a Turing instability in (1.1) where the spatially homogeneous steady state becomes unstable to spatially periodic crime hotspots [4]. Short et al. [7] carried out a weakly nonlinear analysis for one-dimensional and certain two-dimensional (radially symmetric, square and hexagonal) spatially periodic crime hotspots that emerge from the Turing instability of the spatially homogeneous steady state. They also investigated the effect of police suppression on the hotspots and found that if the hotspots exists in the subcritical region then police suppression worked while if the hotspots existed in the supercritical region the police suppression just displaced the hotspots; see also [8].

Beyond domain covering periodic crime hotspots, the possibility of other non-trivial solutions to (1.1) may be of interest in the context of crime hotspots. One particular type of non-trivial solutions that (1.1) may possess are spatially localised solutions[1] that have a sharp spike of high criminal activity surrounded by a region of quiescence. These solutions may account for unexpected crime hotspots where there is no nearby elevated criminal activity above the baseline rate $A^0$ and also crime "spikes" where there may be sudden jumps in criminal activity. These localised hotspots are found to only exist in the subcritical region in parameter space and hence effective police action may help reduce their existence. It is these localised hotspots that are the study of this paper.

Localised "spike" solutions have been previously found and analysed by Kolokolnikov et al. [9]. By noting that $\left(\rho_x - 2\frac{\rho}{A}A_x\right)_x = (A^2(\rho/A^2)_x)_x$, they introduced a change of variable $v = \rho/A^2$ and studied the stationary problem

$$0 = \eta^2 A_{xx} - A + A^0 + vA^3, \tag{1.2a}$$

$$0 = D(A^2 v_x)_x - vA^3 + \bar{A} - A^0, \tag{1.2b}$$

where $D$ is the diffusion coefficient of the criminal density $\rho$ (these equations can be derived from (1.1) via the rescaling $A \to A/D, v \to D^2 v, \bar{A} \to \bar{A}/D, A^0 \to A^0/D$). By looking at the shadowing limit $D \gg 1$ and the singular limit $0 < \eta \ll 1$, they derived the asymptotic spike solution

$$A(x) \sim \begin{cases} \dfrac{2L(\bar{A} - A^0)}{\eta \int w^3} w(x/\eta) & x = \mathcal{O}(\eta), \\ A^0 & x \gg \mathcal{O}(\eta), \end{cases}$$

$$v_0 \sim \frac{(\int w^3 dx)^2}{4L^2(\bar{A} - A^0)^2}\eta^2$$

where $w$ solves $w_{yy} - w + w^3 = 0$ on $y \in [0, L]$. Furthermore, Kolokolnikov et al. were also able to show the existence of multi-pulses and analyse their stability.

While the $D \gg 1$ limit allows for a detailed analysis of the existence and stability of spikes, one would like to know if localised hotspots exist elsewhere in parameter space and also the conditions for their existence e.g. $D = 1$. This would be particularly useful from an application point of view where the diffusion of the criminals is not very fast. One of the main outcomes of this paper is that localised hotspots exist in a far larger region of parameter space than just the $D \gg 1$ limit and that the Turing instability and singular limit ($\eta \to 0$) of (1.1) have a significant effect on the behaviour of the localised hotspots.

Near the Turing instability, one can see that localised patterns should bifurcate off with domain covering periodic patterns away from the shadowing limit. By looking at time-independent solutions, the system (1.1) in one-dimension can be transformed into a fourth-order ODE by solving the first equation for $\rho$ and substituting this into the second equation. Setting $A(x) = B(x) + \bar{A}$, then yields the following equation

$$-\eta^2 B_{xxxx} - 2B_{xx} + 2\frac{B_x^2}{B + \bar{A}} + 4\eta^2 \frac{B_x B_{xxx}}{B + \bar{A}} - 6\eta^2 \frac{B_x^2 B_{xx}}{(B + \bar{A})^2}$$
$$-6A_0 \frac{B_x^2}{(B + \bar{A})^2} + 3\eta^2 \frac{B_{xx}^2}{B + \bar{A}} + 3A_0 \frac{B_{xx}}{B + \bar{A}}$$
$$- \bar{A}B - B^2 + (B + \bar{A})\eta^2 B_{xx} = 0.$$

Carrying out a Taylor series expansion about $B = 0$ and employing the rescaling

$$B \to \frac{u}{\eta^2}, \qquad x \to x\eta\sqrt{\frac{2\bar{A}}{2\bar{A} - \eta^2\bar{A}^2 - 3A^0}},$$

we can re-write the system (1.1) as a single equation (near onset) of the form

$$-(1 + \partial_x^2)^2 u + \left(\frac{4\eta^2\bar{A}^3}{(2 - \eta^2\bar{A} - 3A_0)^2} - 1\right)u$$
$$+ f(u, u_x, u_{xx}, u_{xxx}) = 0,$$

where the function $f = \mathcal{O}(u^2)$ contains all the nonlinear terms (see the appendix (A.2)). Hence near onset, the system (1.1) resembles the quadratic/cubic Swift–Hohenberg equation [10]. From the analysis of the Swift–Hohenberg equation, it is clear that the system undergoes a spatial 1:1 resonance bifurcation of the trivial state $u = 0$ at

$$A^0_* = \frac{2}{3}\bar{A} - \frac{1}{3}\eta^2\bar{A}^2 - \frac{2}{3}\bar{A}\eta\sqrt{\bar{A}}.$$

The normal form theory of Woods & Champneys [11] and Burke & Knobloch [12] can be applied and one can predict the existence of two homoclinic pulses bifurcating off the background state if the bifurcation is subcritical. Near the sub/supercritical transition, one expects homoclinic snaking to exist; see Kozyreff & Chapman [13] and also [11,14–17]. On the plane, localised spots, rings, hexagon fronts and patches have been found in the Swift–Hohenberg equation [18–20].

In this paper, we show that the PDE system (1.1) possesses stationary, spatially localised hotspots on the real line and the plane. In one-dimension, these localised hotspots are found to exist in the subcritical region where a spatially periodic hotspot is modulated by an envelope that decays to the homogeneous background state. Using numerical path-following techniques, we find that these localised hotspots undergo the process of homoclinic snaking where they develop a wider periodic interior region that eventually fills the real line via a sequence of infinitely many folds. This homoclinic snaking creates a region in parameter space where infinitely many localised hotspots co-exist. Interestingly, this homoclinic snaking occurs near the singular limit of the PDE system $\eta = 0$ and hence we analyse both the Turing and singular limits (away from the large-$D$ analysis of [9]) attempting to follow the localised patterns as we pass between the two limits. To the best of the authors' knowledge, this analysis does not appear to have been done before since the most well studied models near singular limits (such as the Gray–Scott model and the Gierer–Meinhardt model) usually do not have a Turing instability.

While the one-dimensional analysis provides some useful insights into the existence of localised hotspots, urban crime is crucially a two-dimensional problem. Hence, in two-dimensions we study the existence of radial spots bifurcating off the spatial homogeneous stead state at $A^0 = A^0_*$ and carry out numerical bifurcation analysis of spots and localised hexagon patterns (both fronts and patches). We find similar behaviour to that observed in the Swift–Hohenberg equation away from the singular limit [18]

[1] Throughout this paper we will use the terms localised states/patterns/solutions/hotspots interchangeably.

while close the singular limit the localised hexagon patterns appear to act like multi-spot solutions much like that seen in one-dimension. Since Short et al. [7] found stable doubly-periodic hexagons, we anticipate that localised hexagon structures may also be stable and of relevance in understanding the PDE model.

While the analysis of the localised patterns is carried out on the real line and plane, we expect these states to persist on large finite-domains and all computations are done on such finite-domains. For $\eta$ away from the singular limit, the effect of finite-domains on the homoclinic snaking scenario has been extensively studied in a range of problems and we expect a similar process to happen here; see for instance [21,22]. Far away and near the singular limit, we anticipate that multiple and appropriately separated copies of the localised hotspots found in this paper can exist and hence be of relevance to understanding crime hotspots.

The paper is outlined as follows. In Section 2, we extend the weakly nonlinear analysis of Short et al. [7] in one-dimension and show that there should be localised hotspots bifurcating off the spatially homogeneous steady state. We then employ numerical continuation to path-follow the localised hotspots and show that they undergo homoclinic snaking in Section 3. We analyse the singular limit in Section 4 and two-dimensional localised patterns (spots and localised hexagons) in Section 5. Finally in Section 6 we draw conclusions and relate the results back to the urban crime context.

## 2. Weakly nonlinear analysis in 1D

In this section we extend the weakly nonlinear analysis of Short et al. [7] to predict the existence of localised pulses; see also [23] for a similar weakly nonlinear analysis for the Swift–Hohenberg equation. We start by noting that the Eqs. (1.1) have the spatially homogeneous equilibrium state

$$A(x,t) = \overline{A}, \tag{2.1}$$

$$\rho(x,t) = 1 - \frac{A^0}{\overline{A}}. \tag{2.2}$$

This state is stable provided $A^0 > A^0_*$ where

$$A^0_* = \frac{2}{3}\overline{A} - \frac{1}{3}\eta^2\overline{A}^2 - \frac{2}{3}\overline{A}\eta\sqrt{\overline{A}}. \tag{2.3}$$

At $A^0 = A^0_*$ there is a Turing instability with the critical wave number given by

$$k_*^2 = \sqrt{\frac{\overline{A}}{\eta^2}}. \tag{2.4}$$

We carry out a weakly nonlinear analysis by setting

$$A^0 = A^0_* - \epsilon\overline{A}, \tag{2.5}$$

and we define a slow time variable $T = |\epsilon|t$. After rescaling $\tilde{x} = |k_*|x$ and dropping reference to tildes, Eqs. (1.1) become

$$|\epsilon|\frac{\partial A}{\partial T} = \eta^2|k_*|^2A_{xx} - A + A^0_* - \text{sign}(\epsilon)\eta^2|k_*|^4|\epsilon| + \rho A \tag{2.6}$$

$$|\epsilon|\frac{\partial \rho}{\partial T} = |k_*|^2\left(\rho_x - \frac{2\rho}{A}A_x\right)_x - \rho A + \eta^2|k_*|^4 - A^0_* + \text{sign}(\epsilon)\eta^2|k_*|^4|\epsilon|. \tag{2.7}$$

We introduce a new slowly varying variable $X = |\epsilon|^{1/2}x$ and expand $A$ and $\rho$ about the spatially homogeneous state

$$A(x,X,T) = \overline{A} + \sum_{j=1}^{\infty}|\epsilon|^{\frac{j}{2}}A^{(j)}(x,X,T), \tag{2.8}$$

$$\rho(x,X,T) = 1 - \frac{A^0_*}{\overline{A}} + \sum_{j=1}^{\infty}|\epsilon|^{\frac{j}{2}}\rho^{(j)}(x,X,T). \tag{2.9}$$

Substituting the previous expressions into Eqs. (2.6) and (2.7), equating coefficients of powers of $|\epsilon|$, Eq. (2.6) yields an expression for $\rho^{(j)}(x,X,T)$ in terms of $\rho^{(j')}(x,X,T)$, $A^{(j)}(x,X,T)$ and their derivatives, where $j'$ represents all the terms less than $j$. By substituting this value for $\rho^{(j)}(x,X,T)$ into Eq. (2.7) and repeating this process generates a series of differential equations of the form,

$$(\nabla^2+1)^2A^{(j)}(x,X,T) = f_j\left[A^{(j')}(x,X,T)\right] \tag{2.10}$$

which can be solved for $A^{(j)}(x,X,T)$.

At order $|\epsilon|^{\frac{1}{2}}$, we have the first equation to solve for

$$(\nabla^2+1)^2A^{(1)}(x,X,T) = 0,$$

from which we find that

$$A^{(1)}(x,X,T) = P(X,T)e^{ix} + c.c.,$$

where $P(X,T)$ is the slowly varying amplitude and $c.c$ denotes complex conjugation.

At order $|\epsilon|$, we find that

$$A^{(2)}(x,X,T) = \frac{4(1-\eta^4k_*^4)}{9\eta^4k_*^6}\left[P^2(X,T)e^{2ix} + c.c.\right].$$

At order $|\epsilon|^{\frac{3}{2}}$ one has to solve

$$(\nabla^2+1)^2A^{(3)} = f_{3,1}[P(T,X);\eta,k_*]e^{ix} + f_{3.2}[P(T,X);\eta,k_*]e^{2ix} + f_{3,3}[P(T,X);\eta,k_*]e^{3ix} + c.c, \tag{2.11}$$

where $f_{3,1}$, $f_{3,2}$ and $f_{3,3}$ are functions, that are not stated for simplicity. Making the secular term $f_{3,1}$ zero (the other secular term $e^{2ix}$ yields an ordinary differential equation for $A^{(2)}$ which is higher order), yields the amplitude equation

$$P_T = \sigma_*P - C_1(\eta,k_*)|P|^2P + \frac{4}{3}\sigma_*\eta^2k_*^2P_{XX}, \tag{2.12}$$

where

$$C_1(\eta,k_*) = \frac{-8+56\eta^2k_*^2-31\eta^4k_*^4-8\eta^6k_*^6}{3\eta^4k_*^8[2\eta^2+\eta^2k_*^2(3-\eta^2)]} \tag{2.13}$$

and $\sigma_*$ is given by the growth rate for the $k_*$ mode, given by $\sigma(k_*) = \sigma_*\epsilon + O(\epsilon^2)$, where

$$\sigma_* = \frac{9\eta^2|k_*|^2}{(1+\eta^2|k_*|^2)[2\eta^2+\eta^2|k_*|^2(3-\eta^2)]}. \tag{2.14}$$

By re-scaling Eq. (2.12), $T \to |\epsilon|t$, $X \to |\epsilon|^{1/2}x$ and defining $Q(t,x) = |\epsilon|^{\frac{1}{2}}P(T,X)$, the amplitude equation can be written as a Ginzburg–Landau equation

$$Q_t = \sigma_*\epsilon Q - C_1(\eta,k_*)|Q|^2Q + \frac{4}{3}\sigma_*\eta^2k_*^2Q_{xx}. \tag{2.15}$$

This equation is known to have stationary real pulse solutions of the form

$$Q = \left(\frac{2\sigma_*\epsilon}{C_1}\right)^{\frac{1}{2}}\text{sech}\left[\left(-\frac{3\epsilon}{4\eta^2k_*^2}\right)^{\frac{1}{2}}x\right] \tag{2.16}$$

provided both $\epsilon$ and $C_1$ are negative i.e. the Turing bifurcation is subcritical (this occurs if $\eta^2k_*^2 \lesssim 0.157$) and where $\sigma_*$ is defined in (2.14); see Short et al. [7].

If $C_1 < 0$ and close to zero, then the analysis can be taken further to yield an amplitude equation of the form (see for example for the Swift–Hohenberg equation Budd & Kuske [23])

$$Q_t = \sigma_*\epsilon Q - C_1(\eta,k_*)|Q|^2Q - C_2(\eta,k_*)|Q|^4Q + \frac{4}{3}\sigma_*\eta^2k_*^2Q_{xx}.$$

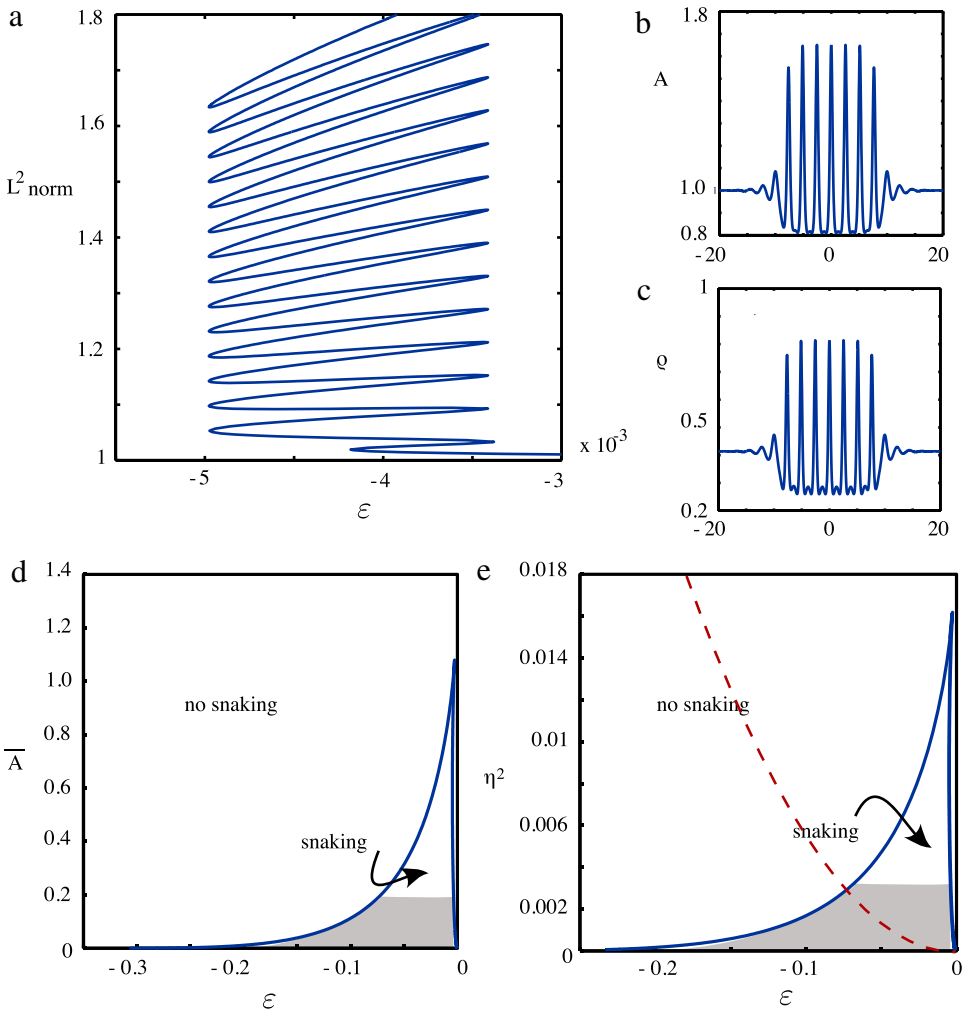


**Fig. 1.** (a) Homoclinic snaking diagram of the 1D PDE system with $\eta^2 = 0.015, \bar{A} = 1A^0 = A^0_* - \epsilon\bar{A}$ with panels (b) and (c) showing the localised pulses in $A(x)$, $\rho(x)$. Two parameter diagrams of the primary fold of the localised patterns are shown in panel (d) with $\eta^2 = 0.015$, and (e) with $\bar{A} = 1$. In panel (e) we also plot the dashed line $\epsilon = -4\eta/3$ denoting the transition where decay to the spatially homogeneous state changes from oscillatory to monotonic decay. The grey regions denote parameter areas where we have been unable to numerically confirm if snaking exists.

This system possesses hysteresis of the pattern state bifurcating off the homogeneous state and a Maxwell point (where a heteroclinic orbit exists) suggesting the existence of homoclinic snaking of the pulse solutions; see Woods & Champneys [11]. We also expect the exponential asymptotics of Kozyreff & Chapman [13] to be valid in this parameter region and expect homoclinic snaking to occur. In Section 3 we will continue the bifurcating pulses and show that homoclinic snaking does exist in this system.

## 3. Homoclinic snaking of pulses

In order to find out what happens to the localised pulses that we found in the previous section, we employ parameter continuation to path-follow the pulses as we vary parameters. To this end, we solve the time-independent system (1.1) using AUTO07P [24] with NTST = 200, spatial truncation = 1000 on the half-line with Neumann boundary conditions. As in [7], we plot just the L2-norm of the attractiveness field

$$\|A\|_2^2 = \int_\Omega (A - \bar{A})^2 d\mathbf{x}.$$

In all the numerics presented in this paper, we set $A^0$ as in (2.5) and continue in $\epsilon$.

In Fig. 1, we path-follow one of the localised pulses with $\eta^2 = 0.015, \bar{A} = 1$ that has bifurcated from the Turing bifurcation and find that we undergo the process of homoclinic snaking where one passes through an infinite sequence of folds where an interior periodic region is grown; see [25] for a description of homoclinic snaking in the Swift–Hohenberg equation. We find that both $A(x)$ and $\rho(x)$ are localised and decay to the spatially homogeneous background state $(A, \rho) = (\bar{A}, 1-A^0/\bar{A})$. We note that the periodic interior of the localised pulses is not strictly sinusoidal like that observed in the Swift–Hohenberg equation [25,26] and we find at the minimum of the pulses the solution rises up a small amount before dropping again and then spiking; see Fig. 1(b) and (c). This "bump" in the pulse near the minimum can be more clearly seen if one decreases $\eta$ as shown in Fig. 2. In Fig. 2, we see that the pulse in the $A$ variable starts at the spatially homogeneous value $\bar{A}$, decreases to a minimum value that is approximately $A = A^0$ before going on a large spike where it returns to the minimum value $A \sim A^0$ and the little bump rises back towards $\bar{A}$ before decreasing again and another spike occurs.

Fig. 2 also shows how the width of the pulses are grown as one proceeds around the bifurcation diagram. Starting at the right fold, two new spikes are grown at either ends of the interior region as one transverses the snake to the left. Once the left fold is reached, the solution remains almost the same until one reaches a right fold

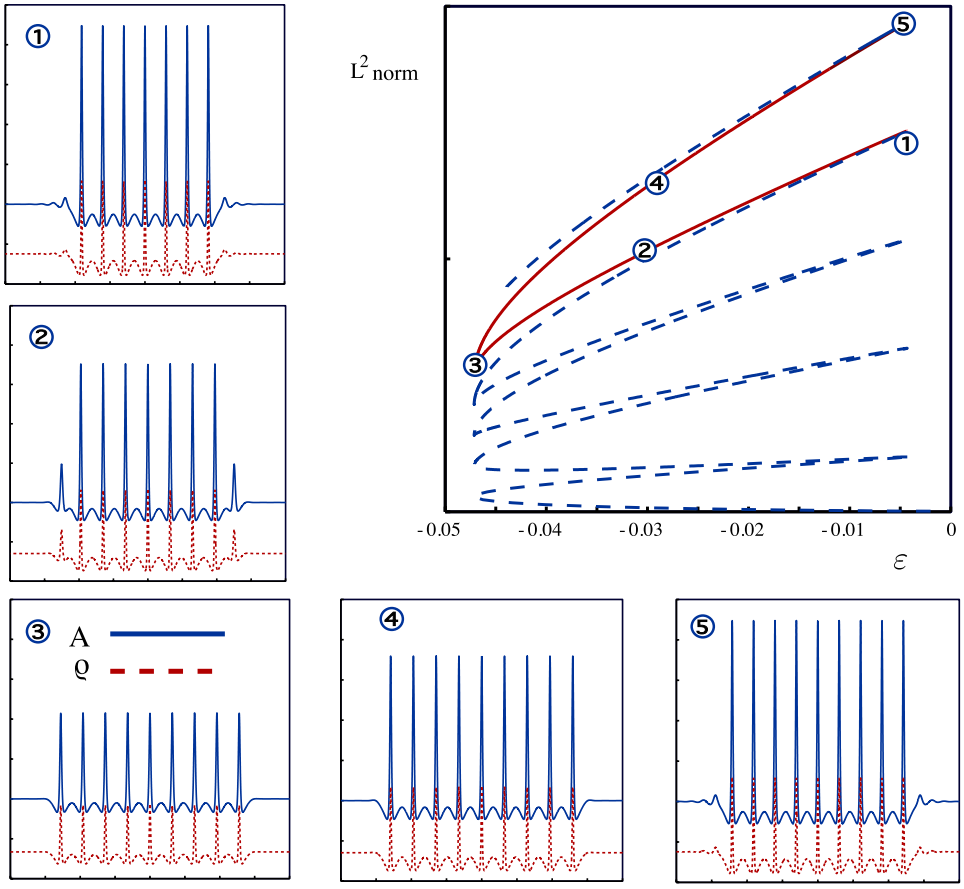


**Fig. 2.** Bifurcation diagram with $\eta^2 = 0.005$. As one goes from right to left on the bifurcation diagram, spikes are grown. We note that the spatial eigenvalues of the spatially homogeneous state remain complex throughout the snaking region.

again. At the left fold the decay to the spatially homogeneous state appears to be monotonic unlike at the right fold. For the parameter values in Fig. 2, we find the background state has oscillatory decay until $\epsilon \sim -0.094$ and so for the entire snaking region in Fig. 2 the decay to the spatially homogeneous state is oscillatory.

In general, the spatial eigenvalues of the background state for $\overline{A} = 1$, are given by

$$\lambda_{1,2} = \pm\frac{\sqrt{2}}{2\eta}\sqrt{-3\epsilon - 2\eta + \sqrt{9\epsilon^2 + 12\eta\epsilon}},$$
$$\lambda_{3,4} = \pm\frac{1}{2\eta}\sqrt{-6\epsilon - 4\eta - 2\sqrt{9\epsilon^2 + 12\eta\epsilon}}.$$

From these eigenvalues, we see that there are three possibilities

- $\epsilon < -4\eta/3$, the eigenvalues are all real,
- $-4\eta/3 < \epsilon < 0$, the eigenvalues are all complex,
- $\epsilon > 0$, the eigenvalues are all imaginary.

In Fig. 1(e), we plot the (dashed) line $\epsilon = -4\eta/3$ separating the region where the decay to the background state changes from oscillatory to monotonic decay. It appears there does exist a region in parameter space (for $\eta^2 < 0.003$) where the type of decay to the homogeneous state changes within the snaking region. While this change in the type of decay should have little effect on the homoclinic snaking it could have a significant impact on multi-pulses (states that are form of two or more weakly interacting localised patterns that include a periodic interior) as decay to the background state has a significant effect on the existence regions of multi-pulses away from the singular limit $\eta \to 0$; see [27,28]. In Fig. 1(d) and (e), we plot the continuation of a left and right fold of the snaking region in two parameters. We find that as we decrease either $\overline{A}$ or $\eta$, the width of the snaking region increases. Of particular interest is the fact that the snaking region seems to coincide with the singular limit $\eta = 0$ of the system. For $\eta^2 < 0.005$, the numerics become very stiff due to the large gradients in the solution but we do see a primary fold of the pulse solutions but the upper branch terminates at $\epsilon \sim 0$ where the numerics fail to converge.

We now preempt some of the singular limit analysis carried out in Section 4 by looking at what happens to the localised solutions starting from the snaking region as we decrease $\eta$. From the singular limit analysis in Section 4, we find that it is useful to plot the solutions in $(A, B, v, w)$-variables where $B = A_y$, $v = \rho/A^2$, $w = A^2 v_y$ and $x = \eta y$. In Fig. 3, we show two solutions for different values of $\eta$. We see in Fig. 3(a) and (b), that as $\eta$ is decreased the distance between the spikes increases, the maximum of the "bumps" between the spikes approach the spatially homogeneous background state and the solutions approach what appears to be a multi-pulse state. It is not expected that such multi-pulse solutions undergo homoclinic snaking [29] and hence we believe that snaking ceases as one approaches the singular limit.

Fig. 3(d) also shows how the localised solutions scale as $\eta$ is decreased. We see that the height of the spikes scale like $\sim 1/\eta$, while the value of $v$ during the spikes scales like $\sim\eta^2$ and the jump in $w$ converges to a constant that is $\sim 0.6$. We will use these scalings in the singular limit analysis in Section 4.

In the next section, we investigate the singular limit to explain the structure of the solutions found near $\eta = 0$.

## 4. Singular limit analysis

In this section, we investigate the singular limit $\eta = 0$ and attempt to explain some of the properties of the pulses observed in

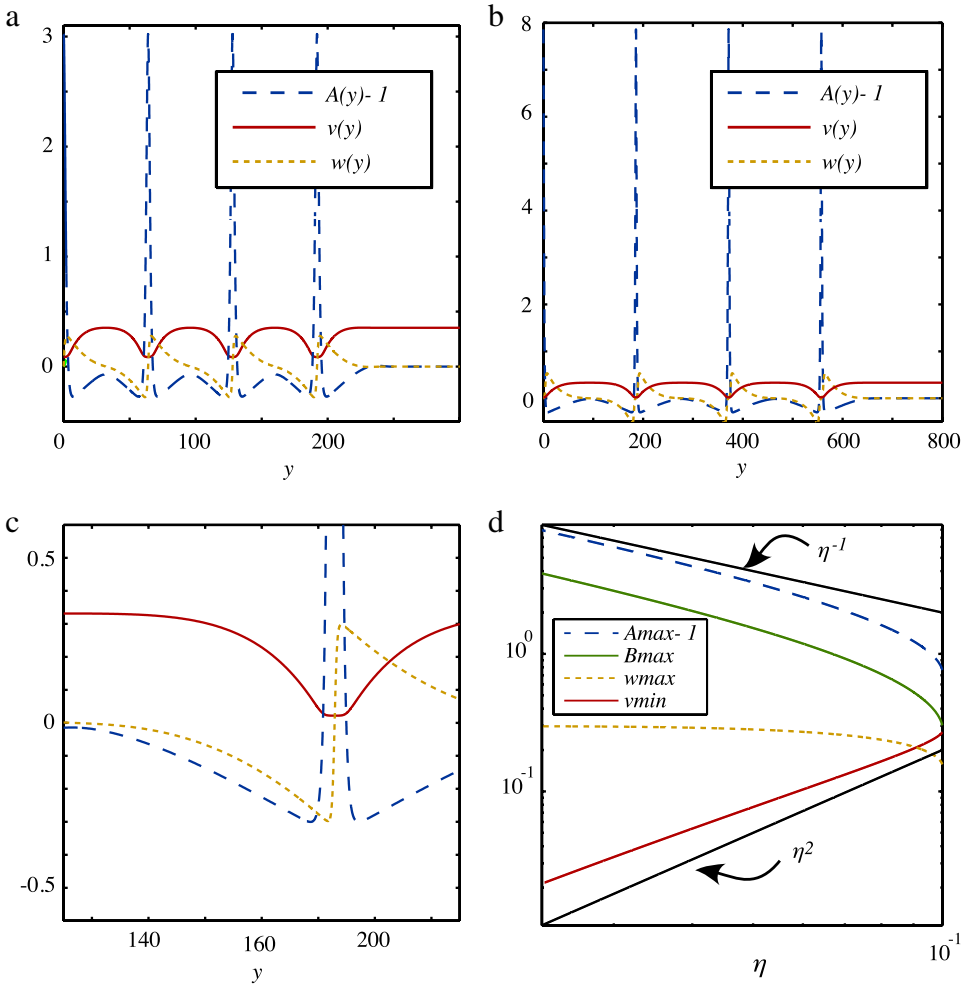


**Fig. 3.** Localised solutions in $(A, v, w)$-variables for the parameters $\bar{A} = 1, \epsilon = -0.018$ (a) $\eta = 0.054$, (b) $\eta = 0.023$, and (c) Zoom-in of the box in panel (b). From this it is clear that $v$ is a constant during the fast phase while $w$ is clearly varying rapidly. (d) Log–log plot of the scalings of the max of $A$, $B$ and $w$ and min of $v$. We find $\max(A)$, $\max(B)$ scale $\sim 1/\eta$ while $\min(v)$ scales $\sim \eta^2$ and $\max(w)$ is independent of $\eta$.

the previous section that are not captured by the large-$D$ analysis of [9]. We employ the change of variables $v = \rho/A^2$, and re-write (1.2) as a first order ODE system to yield

$$\eta A_x = B, \tag{4.1a}$$

$$\eta B_x = A - vA^3 - A^0, \tag{4.1b}$$

$$v_x = \frac{w}{A^2}, \tag{4.1c}$$

$$w_x = vA^3 - \bar{A} + A^0, \tag{4.1d}$$

where

$$A^0 = \left(\frac{2}{3} - \epsilon\right)\bar{A} - \frac{1}{3}\eta^2\bar{A}^2 - \frac{2}{3}\eta\bar{A}\sqrt{\bar{A}}, \tag{4.2}$$

since we wish to investigate the interaction of the Turing instability with $\epsilon < 0$ in the region where the spatially homogeneous state is temporally stable. We call (4.1) the *slow system*.

We re-scale space via $x = \eta y$ to yield the *fast system*

$$A_y = B, \tag{4.3a}$$

$$B_y = A - vA^3 - A^0, \tag{4.3b}$$

$$v_y = \eta\frac{w}{A^2}, \tag{4.3c}$$

$$w_y = \eta\left[vA^3 - \bar{A} + A^0\right]. \tag{4.3d}$$

In these coordinates, we have the spatially homogeneous equilibrium given by

$$A = \bar{A}, \qquad B = 0,$$
$$v = \bar{v} = \frac{\bar{A} - A^0}{\bar{A}^3} = \frac{\left(\frac{1}{3} + \epsilon\right) + \frac{1}{3}\eta^2\bar{A} + \frac{2}{3}\eta\sqrt{\bar{A}}}{\bar{A}^2}, \qquad w = 0.$$

We note that both the fast and slow systems possess the symmetry

$$\begin{aligned} &x \to -x, \qquad y \to -y, \qquad A \to A, \\ &B \to -B, \qquad v \to v, \qquad w \to -w. \end{aligned} \tag{4.4}$$

We wish to find homoclinic orbits with this symmetry that correspond to the spike solutions in Fig. 3 (the individual spike solutions possess this symmetry).

We will first look at the slow and fast limits at $\eta = 0$ and then carry out the matching.

### 4.1. Slow system analysis

Setting $\eta = 0$ in (4.1), the reduced slow subsystem is defined only on the invariant plane

$$\mathcal{M}_0 = \left\{v, w, B = 0, A - vA^3 - A^0 = 0\right\},$$

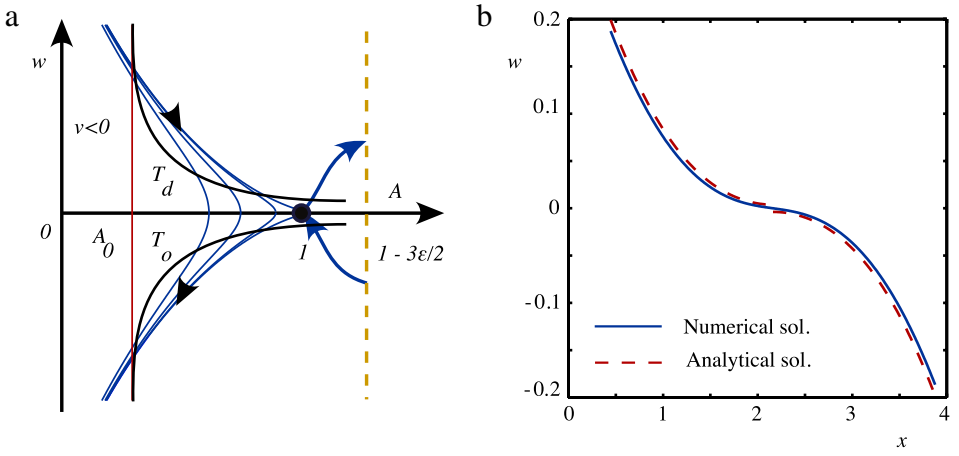


**Fig. 4.** (a) Phase space of the slow system with $\bar{A} = 1$, $A^0 = (2/3 - \epsilon)$ and (b) plot of the numerical solution $w(x)$ for $\eta = 0.023$ against the analytical solution (4.7) with $\Theta = -3\epsilon$ using the numerical $A(x)$ field.

and is given by

$$v_x = \frac{w}{A^2},$$
$$w_x = vA^3 - \bar{A} + A^0.$$

Firstly, we note that the cubic polynomial in $A$ can be re-written to find

$$v = \frac{A - A^0}{A^3} \tag{4.5}$$

and hence for $v > 0$ (and the solutions to remain well posed) we require that $A > A^0 = (2/3 - \epsilon)\bar{A}$.

Using (4.5), we re-write the slow subsystem in terms of $A$ and $w$ to yield

$$A_x = \frac{A^2 w}{(3A^0 - 2A)}, \tag{4.6a}$$
$$w_x = A - \bar{A}. \tag{4.6b}$$

This system has a saddle equilibrium at $E : (A, w) = (\bar{A}, 0)$. There is a singularity in the vector field at $A = 3A^0/2$ but since $\epsilon < 0$ this is away from the region of interest. The phase portrait of the slow subsystem is shown in Fig. 4(a).

From the phase portrait shown in Fig. 4(a), we solve the system where $A$ is a graph of $w$ i.e., $A = f(w)$, yielding the single ODE

$$\frac{df}{dw} = \frac{f^2 w}{(3A^0 - 2f)(f - \bar{A})},$$

which can be integrated to yield

$$-2A + 3\ln(A)A^0 + 2\ln(A)\bar{A} + 3\frac{A^0\bar{A}}{A} = \frac{1}{2}w^2 + \Theta, \tag{4.7}$$

where $\Theta$ is an integration constant to be determined by the initial conditions.

We can find the (un)stable manifolds of the steady state by setting $(A, w) = (\bar{A}, 0)$ in (4.7) to find $\Theta$

$$\Theta = 3A^0 - 2\bar{A} + \ln(\bar{A})(3A^0 + 2\bar{A}). \tag{4.8}$$

In the special case when $\bar{A} = 1$, we find $\Theta = -3\epsilon$. Therefore, we define the stable and unstable manifolds of the equilibrium $E$ restricted to $\mathcal{M}$ as

$$W^{U,S}(E)|_{\mathcal{M}} : w = \pm\sqrt{2\left(-2A + 3\ln(A)A^0 + 2\ln(A)\bar{A} + 3\frac{A^0\bar{A}}{A} - \Theta\right)} =: \sqrt{f(A)}, \tag{4.9}$$

where $\Theta$ is defined in (4.8).

In Fig. 4(b), we compare the analytical solution (4.7) (with $\bar{A} = 1$, $\Theta = -3\epsilon$) with the numerical solution during the "periodic" interior of the localised pulse for $\eta = 0.023$ and find an excellent agreement. As $\eta$ is decreased, the numerical solution appears to converge to the analytical solution $\Theta = -3\epsilon$ that connects the spatially homogeneous state.

In Fig. 4(a), we also plot the take-off and touch-down curves where trajectories leave and enter the slow manifold (these curves are calculated in Section 4.3) Eqs. (4.20). We see that the take-off and touch-down curves asymptote at $A = A^0$ and we expect the take-off and touch-down points to occur at $A \sim A^0$ i.e., $v \sim 0$. We will use this fact in the analysis of the fast system.

### 4.2. Fast system analysis

The fast subsystem (4.3) for $\eta = 0$ is given by

$$v(y) = v_0, \qquad w(y) = w_0, \qquad A_{yy} = A - vA^3 - A^0. \tag{4.10}$$

This system has a homoclinic orbit to $A \sim A^*$ where $A^*$ solves the cubic polynomial $A^* - v_0(A^*)^3 - A^0 = 0$, and

$$A^* = -\frac{1}{12}\frac{\alpha^{1/3}}{v_0} - \frac{1}{\alpha^{1/3}} - \frac{i\sqrt{3}}{2}\left(\frac{\alpha^{1/3}}{6v_0} - \frac{2}{\alpha^{1/3}}\right)^{1/3} \tag{4.11}$$

where

$$\alpha = \left(-108A^0 + 12\sqrt{\frac{3(27(A^0)^2 v_0 - 4)}{v_0}}\right)v_0^2.$$

The right-hand side of (4.11) is real-valued provided that $v_0 \le \bar{v}$. The existence of a homoclinic to $A^*$ in the fast sub-system explains the spiking in the interior of the localised pulses in the $A$ variable shown in Section 3. We note that the fast system (4.3) for $\eta = 0$, possesses a Hamiltonian

$$H(A, B; v) = \frac{B^2}{2} - \frac{A^2}{2} + \frac{vA^4}{4} + A^0 A,$$

and we can calculate the splitting distance between the manifolds $W^S(\mathcal{M})$ and $W^U(\mathcal{M})$ via the Melnikov integral

$$\Delta H(v_0, w_0; A^0, \bar{A}) = \int_{-\infty}^{\infty} \dot{H}(A(y), B(y), v(y), w(y))dy = \frac{\eta}{4}\int_{-\infty}^{\infty} w(y)A(y)^2 dy. \tag{4.12}$$

Hence, for the splitting distance to be zero we require that $A$ is an even function and $w$ is an odd function i.e. $w_0 = 0$. Since we

require $w_0 = 0$, in order to be able to match the fast manifold with the slow manifold we require that $A^* \approx \bar{A}$ (so that $w$ remains close to zero from the slow manifold) and hence $v_0 \approx \bar{v}$ for $0 < \eta \ll 1$. In particular, we expect $v_0$ to be $\mathcal{O}(\eta)$ less than $\bar{v}$. This situation appears to be almost exactly the same geometrically to that studied for the Gray–Scott model [30] and we will show numerically in Section 4.3 that these pulses exist. Unfortunately, there is no explicit form for the homoclinic orbit of (4.10) making a more detailed analysis difficult and so we do not attempt to carry it out here.

From Fig. 3, we see that there also exists solutions where $v$ is very small ($\sim\eta^2$) during the fast phase while there is a sharp $\mathcal{O}(1)$ jump in $w$ from positive to negative values. Initially, it may look like one cannot match the fast and slow manifolds for these solutions but due to the $v$ term being small during the fast-phase (resulting in a large spike), it turns out that $w$ becomes order one.

We start by find an expansion that is consistent with the numerics of the fast subsystem (4.10) to leading order for small $v_0$ by first shifting $A$ as follows

$$A(y) = A^* + C(y),$$

and rescaling $C = \tilde{C}/\sqrt{v_0}$ to yield

$$\tilde{C}_{yy} = \tilde{C} - \tilde{C}^3 + \mathcal{O}(\sqrt{v_0}). \tag{4.13}$$

Assuming $v_0 \ll 1$, we find to leading order

$$\tilde{C} = \sqrt{2}\,\mathrm{sech}(y).$$

Next we find the influence of this leading order fast phase solution on the slow variables $v$ and $w$ by calculating

$$\begin{aligned}\Delta v(y) &= \eta \int_{-y^*}^{y^*} v_y dy \\ &= \eta \int_{-y^*}^{y^*} \left[\frac{\sqrt{v_0} w}{(\tilde{C} + \sqrt{v_0}A^*)^2}\right] dy + \text{h.o.t}, \end{aligned} \tag{4.14a}$$

$$\begin{aligned}\Delta w(y) &= \eta \int_{-y^*}^{y^*} w_y dy \\ &= \eta \int_{-y^*}^{y^*} \left[\frac{\tilde{C}^3}{\sqrt{v_0}} + \tilde{C}^2 A^* - \bar{A} + A^0\right] dy + \text{h.o.t}, \end{aligned} \tag{4.14b}$$

where $1 \ll y^* \ll \mathcal{O}(1/\eta)$ is the matching point (we will discuss below why we cannot take $y = \mathcal{O}(1/\eta)$). Since we are looking for solutions that are odd in $w$ and even in $\tilde{C}$, we find that $\Delta v$ is zero to leading order. For there to be an $\mathcal{O}(1)$ change in $w$ during the fast phase as $\eta \to 0$, we require that $v_0 \sim \eta^2$. This matches with the numerical scalings found in Section 3. We proceed by setting $v_0 = \eta^2 \tilde{v}_0$ and find the leading order influence on $\Delta w$ to be for large $y^*$

$$\Delta w \approx \int_{-\infty}^{\infty} \left[\frac{2\sqrt{2}\,\mathrm{sech}^3(y)}{\sqrt{\tilde{v}_0}}\right] dy = \pi\sqrt{\frac{2}{\tilde{v}_0}}. \tag{4.15}$$

Assuming $v(y) = \eta^2\tilde{v}_0$, we can integrate the equation for $w$ to find a leading order approximate solution for the fast phase given by

$$A(y) = A^* + \frac{1}{\eta}\sqrt{\frac{2}{\tilde{v}_0}}\,\mathrm{sech}(y), \tag{4.16a}$$

$$\begin{aligned} w(y) &= \sqrt{\frac{2}{\tilde{v}_0}}\left(\frac{\sinh(y)}{\cosh(y)^2} + 2\mathrm{atan}(e^y) - \frac{1}{2}\pi\right) \\ &\quad - \eta(\bar{A} - A^0)y + A^*\eta\tanh(y). \end{aligned} \tag{4.16b}$$

In Fig. 5, we plot the numerics of the same pulses but in this new re-scaled system and observe that the quantities max $A$, $B$, $w$ and min $v$ do not change as $\eta$ is decreased. We also overlay the analytical solutions of the fast system by taking $v_0$ from a numerical solution at the origin and find a reasonable match during the fast excursion for small $y$.

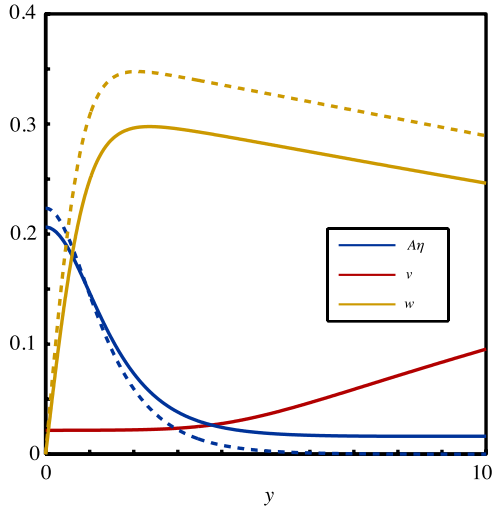


**Fig. 5.** Comparison with fast system numerics (solid lines) and the analytical solution (4.16) for $A$ and $w$ with parameters $\epsilon = -0.018$, $\eta = 0.028$. The dashed lines are the singular limit solution (4.16). The value of $v_0$ is taken to be the minimum value of $v$ of a computed solution at $y = 0$.

Let us discuss the validity of the jump calculations and the expansion (4.16). Kolokolnikov et al. [9] showed that in the $D \gg 1$ limit one needs to carry out a two-term expansion for the fast phase if $v \sim \mathcal{O}(\eta^2)$. In our case, such an expansion yields

$$v \sim \eta^2\tilde{v}_0 + \eta^3\left(\frac{\pi\sqrt{\tilde{v}_0}e^{2y}}{32} + \tilde{v}_1\right),$$

for large $y$, where $\tilde{v}_0$ and $\tilde{v}_1$ are constants to be found from the matching. Due to the exponentially growing term, such an expansion is valid only until $y \sim \mathcal{O}(\log(1/\sqrt{\eta}))$. Furthermore, carrying out the two term expansion as in [9] yields $A \to -\infty$ as $y \to \infty$ suggesting a more sophisticated analysis is required for the fast-phase. However, the jump in $w$ will be governed by the leading order term provided we do not take $y^*$ too large and it is this variable that we will attempt to match with the slow-phase.

### 4.3. Matching

In this section, we formally match the fast and slow manifolds and construct a single pulse to the equilibrium $E$ by finding $v_0$. We first show that the slow manifold is normally hyperbolic and hence standard matched asymptotics is applicable in this situation.

The condition for the slow manifold to be normally hyperbolic comes from the linearisation of the fast system with respect to $A$, $B$-variables given by $\dot{\mathbf{x}} = J(A, B)\mathbf{x}$, where

$$J(A, B) = \begin{bmatrix} 0 & 1 \\ 1 - 3vA^2 & 0 \end{bmatrix},$$

and $\mathbf{x} = [A, B]^T$. The slow manifold will be normally hyperbolic if $J$ is hyperbolic i.e.

$$A < \frac{1}{\sqrt{3v}}.$$

Substituting (4.5) into this condition, we find that the slow manifold is normally hyperbolic if

$$A < \frac{3}{2}A^0 = \frac{3}{2}\left(\frac{2}{3} - \epsilon\right)\bar{A}.$$

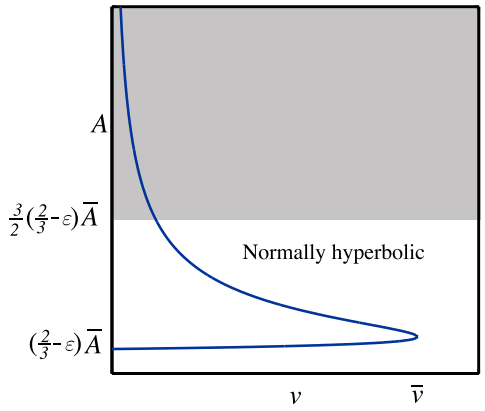


**Fig. 6.** Plot of the cubic polynomial $A - vA^3 - \left(\frac{2}{3} - \epsilon\right) = 0$ and the region where the invariant plane $\mathcal{M}_0$ is normally hyperbolic.

Since, we are in the subcritical region (i.e., $\epsilon < 0$), the hyperbolic part of the slow manifold also contains the homogeneous equilibrium $(A, B, v, w) = (\bar{A}, 0, \bar{v}, 0)$.

In Fig. 6, we plot the cubic polynomial and show where the region where the plane $\mathcal{M}_0$ is normally hyperbolic. We note that we wish to match in the region where $v \leq \bar{v}$ (since from the slow manifold analysis $v$ is decreasing from $\bar{v}$) and hence the region of the slow manifold we are interested in is normally hyperbolic provided $\epsilon < 0$ on the compactified manifold with $0 \leq v \leq \bar{v} + \epsilon$. Fenichel's theory [31] implies that there exists an slow manifold $\mathcal{M}$, for $0 < \eta \ll 1$, that remains invariant under the flow of the full system and is $\mathcal{O}(\eta)$-close to $\mathcal{M}_0$.

We first recall from Section 4.2 that a possible matching is

$$v_0 \approx \bar{v} = \frac{\bar{A} - A^0}{\bar{A}^3}. \tag{4.17}$$

Looking at the relation (4.2) for $A^0$, we find that $v_0 \to 0$ as $\epsilon \to -1/3$. When this occurs, we expect that another localised state can be constructed.

We will now show formally that another localised state to $\bar{A}$ can be constructed for $v_0 \ll 1$. We first note that the homoclinic orbit for $A$ converges to the equilibrium $A^*$ (4.11) which for small $v_0$ has the following expansion

$$A^* = A^0 + (A^0)^3 v_0 + \mathcal{O}(v_0^2). \tag{4.18}$$

This is a point on the slow manifold $\mathcal{M}_0$ defined by the relation (4.5)

$$v = \frac{A^* - A^0}{(A^*)^3} = v_0 + \mathcal{O}(v_0^2). \tag{4.19}$$

Hence, the slow $v$-variable matches with the fast $v_0$-variable to leading order.

We now consider a trajectory starting in the fast field with initial conditions

$$(A(0), B(0), v(0), w(0)) = (A(y = 0; v), 0, \eta^2 \tilde{v}_0, 0),$$

and we evolve the fast system until $y = y^* \sim \mathcal{O}(\log(1/\sqrt{\eta})) \gg 1$. To leading order $A(y^*) = A^* \approx A^0$. At this point there is a jump onto the slow manifold with values $(v_0^+, w_0^+)$. Hence, we may define the *touch-down* curve $T_d$ (and similarly in backwards time a *take-off* curve $T_o$) where solutions land on the slow manifold to be to leading order

$$T_d: \; w = +\frac{1}{2}\Delta w = +\frac{\pi}{2}\sqrt{\frac{2}{\tilde{v}_0}}, \tag{4.20a}$$

$$T_o: \; w = -\frac{1}{2}\Delta w = -\frac{\pi}{2}\sqrt{\frac{2}{\tilde{v}_0}}, \tag{4.20b}$$

where we have used $\Delta w$ defined in Eq. (4.15). We note that the matching point on the slow manifold $(v_0^+)$ is found from (4.19) to be $v_0^+ = \eta^2 \tilde{v}_0$ and since we have imposed the condition $w(0) = 0$, we require the value of $w$ at the matching point from the slow field $(w_0^+)$ is given, to leading order, by

$$\begin{aligned} w_0^+ &= \sqrt{2\left(-2A^0 + 3\ln(A^0)A^0 + 2\ln(A^0)\bar{A} + 3\bar{A} - \Theta\right)} \\ &= \sqrt{f(A^0)}, \end{aligned}$$

as we wish to match with the stable manifold of the spatially homogeneous equilibrium on the slow manifold (4.9). Hence, we find to leading order

$$\tilde{v}_0 = \frac{\pi^2}{2f(A^0)}, \tag{4.21}$$

where $\Theta$ is the arbitrary constant in (4.7). Since we have taken the initial conditions of our trajectory to be $B(0) = 0$, $w(0) = 0$, then using the symmetry (4.4) we can construct a similar trajectory evolving backwards in time and construct a unique localised homoclinic pulse to $(A, B, w, v) = (\bar{A}, 0, \bar{v}, 0)$ provided that $A^0 > A^0_*$. In Fig. 7(a), we draw a schematic sketch of the phase space with the take-off and touch-down curves in the slow field. Graphically, we find the intersection of the stable and unstable manifolds of $E$ with the take-off and touch-down curves to be at $A \sim A^0$. We also plot the comparison of the asymptotic $\tilde{v}_0^+$ value (4.21) with the numerically calculated $\tilde{v}_0 = \min(v)/\eta^2$ in Fig. 7(b) for $\eta^2 = 1 \times 10^{-7}$, $\bar{A} = 1$ with $A^0$ set as in (2.5). We see that the numerically calculated value of $\tilde{v}_0$ starts ∼50 and increases until is undergoes a fold around $\epsilon = -0.32$ by which point $\tilde{v}_0$ is no longer $\mathcal{O}(\eta^2)$. For small values of $\tilde{v}_0$, we find the approximation (4.21) to be excellent while for large values of $\tilde{v}_0$ the approximation (4.17) fits well. The upper part of the branch in Fig. 7(b) is the branch that initially bifurcates off the spatially homogeneous steady state at the Turing bifurcation point $\epsilon = 0$. Looking at the intersection of the two approximations for $\tilde{v}_0$ (4.21) and (4.17) we find that the predicted fold should occur at $(\epsilon, \tilde{v}_0) = (-0.3248, 64139)$ that is of the same order of magnitude as the numerically calculated fold at $(\epsilon, \tilde{v}_0) = (-0.3178, 40530)$.

Formally, we can construct multi-pulse solutions by 'glueing' several of the single localised pulses together provided they are well separated. It is these solutions (involving the large spike) that numerically we seem to be converging to as $\eta \to 0$ as seen in Fig. 3. It is not clear from the analysis or the numerics whether homoclinic snaking in the singular limit can be ruled out and we leave this as an open problem.

We note that there are several problems with this matching. Firstly, we do not have a good uniform expansion for the fast phase (in particular for the $v$ variable) as discussed in Section 4.2. Furthermore, it is not clear that when $\eta > 0$, the $\mathcal{O}(\eta)$-perturbation to the slow manifold $\mathcal{M}_0$ will mean that $v$ can no longer be matched with the fast phase due to $v_0 \sim \mathcal{O}(\eta^2)$. This appears to be a complicated problem where more sophisticated methods are required; see Kolokolnikov et al. [9, Section 5] and references therein. Secondly, we have a gap in the matching as the fast system analysis suggests we can only match at $y = y^* \sim \mathcal{O}(\log(1/\sqrt{\eta}))$. We believe that a more delicate analysis is required in order to resolve both these issues.

## 5. Two-dimensional localised patterns

In this section we investigate localised spots and hexagon patterns near the Turing instability and the singular limit ($\eta \to 0$) using our knowledge from the one-dimensional calculations in the previous sections. We start by looking at bifurcating spots from the Turing instability where the bifurcation theory of Lloyd & Sandstede [19] and McCalla [32] applies. Using numerical continuation, we trace out the bifurcation diagram for the spots. In Sections 5.2 and 5.3, we investigate numerically the bifurcation structure of the localised hexagon states.

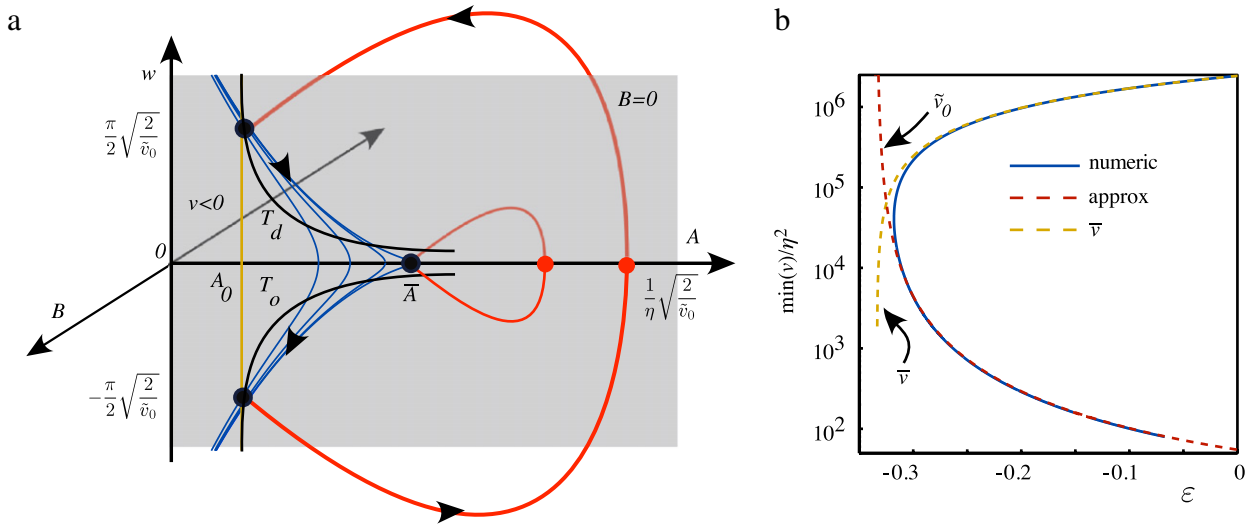


**Fig. 7.** (a) Schematic sketch of the phase space of the system. (b) Comparison of the numerically computed $\min(v)/\eta^2$ (solid blue) with the analytical estimates for $\widetilde{v}_0$ (dashed lines) for $\eta^2 = 1 \times 10^{-7}$, $\bar{A} = 1$ with $A^0$ set as in (2.5).

### 5.1. Spots

Near a Turing instability in general Reaction–Diffusion systems, three types of stationary, radially symmetric localised solutions have been proven to exist: a localised ring decaying to almost zero at the core $r = 0$, a spot with a maximum (called Spot A) at $r = 0$ and a spot with a minimum at $r = 0$ (called Spot B); see Lloyd & Sandstede [19] and McCalla and Sandstede [20,32]. In Fig. 8, we plot a Spot A, and in Fig. 8(d) we plot a Spot B and Fig. 8(e), we plot a ring. The existence of these radial solutions near a Turing instability relies on carrying out a radial centre-manifold of Scheel [33] to yield a quadratic/cubic Swift–Hohenberg equation on the centre-manifold. Provided the quadratic term in the Swift–Hohenberg equation is non-zero i.e., up–down symmetry is broken at onset, the existence of Spot A can be rigorously established.

We only establish the existence of a stationary Spot A near a Turing instability for Eq. (1.1) in Theorem 1 as these localised patterns are the most interesting from an application point of view since we find that these small amplitude spots undergo a fold as $\epsilon$ is decreased and become finite amplitude crime hotspots; the proof is an adaptation of Theorem 2 in [19] and establishes the non-degeneracy condition for a Spot A to bifurcate from the spatial homogeneous steady state, see the Appendix for details.

**Theorem 1.** *Fix $\bar{A}$, $\eta > 0$, then provided*

$$\begin{aligned}\theta = {} & \frac{\alpha^4}{\eta^4}\frac{4}{\sqrt{3}} - \frac{2}{\sqrt{3}}\frac{\alpha^2}{\eta^4}\left(\frac{3A^0_*}{\bar{A}^2} - \eta^2\right) \\ & - \frac{8}{\bar{A}\eta^2}\left(-\frac{2}{\sqrt{3}} - \frac{10\pi}{3} - \sqrt{3}\right) + \frac{1}{\bar{A}\eta^2}\left(\frac{8\pi}{3} + \sqrt{3}\right) \\ & + 2\frac{\alpha^2}{\eta^4\bar{A}}\left(\frac{6A^0_*}{\bar{A}} - 1\right)\frac{2}{\sqrt{3}} + \frac{\alpha}{\eta^4\bar{A}}(3A^0_* - 10\eta^2)\left(\frac{2}{\sqrt{3}} - 2\pi I_1\right) \\ & - \frac{6}{\eta^2\bar{A}}\left(\frac{4}{\sqrt{3}} + \frac{4\pi}{3} + \sqrt{3}\right) - \frac{\alpha^2}{\eta^2}\left(\frac{2\pi}{3} - \frac{4}{\sqrt{3}}\right) \neq 0,\end{aligned}$$

*where $\alpha = \sqrt{\eta/\sqrt{\bar{A}}}$ and $I_1 = \int_0^\infty J_0(r)J_1(r)^2 dr \sim 0.186$, then for some $\epsilon_* > 0$ with $A^0 = A^0_* + \epsilon$ for $\epsilon \in (0, \epsilon_*)$, there exists a stationary localised spot that bifurcates from the spatially homogeneous state $(A, \rho) = (\bar{A}, \bar{\rho})$ of (1.1) and for each fixed $r_* > 0$, we have the asymptotics $A = \bar{A} + \beta\sqrt{\epsilon}J_0(r) + \mathcal{O}(\epsilon)$ uniformly in $0 \le r \le r_*$ for an appropriate constant $\beta = \mathcal{O}(1)$ and $\text{sign}(\beta) = -\text{sign}(\theta)$.*

We find numerically, that for almost all parameter values, one can expect localised spots to bifurcate off the spatially homogeneous state at the Turing instability $A^0 = A^0_*$. In particular, for $\eta \ll 1$ the leading order term in $\theta$ is given by

$$\theta \sim 3\frac{A^0_*\alpha}{\bar{A}\eta^4}\left(\frac{2}{\sqrt{3}} - 2\pi I_1\right) < 0. \tag{5.1}$$

Spot B and localised rings are also expected to bifurcate off the spatially homogeneous state $(A, \rho) = (\bar{A}, \bar{\rho})$ provided that the coefficient $C_1(\eta, k_*) < 0$ from Section 2 i.e., the 1D Turing bifurcation is subcritical; see [32].

The singular perturbation analysis carried out in Section 4 can be adapted to the radial case where we find a pulse in the $A$ variable similar to that in [9]. However, the slow system does not appear to have an explicit analytical solution and so the locations of the stable and unstable manifolds are not known making matching difficult. However, we are able to make some observations. Firstly, the leading order fast system where $r = \eta s$ for $\eta = 0$ is given by

$$v(s) = v_0, \qquad w(s) = w_0, \qquad A_{ss} + \frac{1}{s}A_s = A - vA^3 - A^0. \tag{5.2}$$

Similar to the discussion in Section 4.2, seeking solutions that are odd in $w$ yields that

$$w_0 \approx 0, \qquad v_0 \approx \bar{v} = \frac{\bar{A} - A^0}{\bar{A}^3}, \tag{5.3}$$

to leading order. We expect solutions of (5.2) to be a good description of the radial spot branch until $\bar{v} = 0$ (i.e., when $\epsilon \approx 1/3$) at which point we expect a fold. For $v_0 \ll 1$, a far more delicate analysis is required in order to predict the spots and we do not do this here.

We now numerically solve the stationary system (1.1) in radial coordinates in AUTO07P [24] with NTST = 1000, and a domain truncation of 1000 on the half line with Neumann boundary conditions. In Fig. 8, we show the bifurcation diagrams for the radial spot A as we path-follow the spot bifurcating from the Turing instability. Here we see that the radial spot exists over a significantly larger region in parameter space than the one-dimensional pulse as already noted by Short et al. [7]; compare with Fig. 1(a). As one moves away from the Turing instability, the decay to spatially homogeneous state changes from oscillatory to monotonic and the spot resembles the spike solution found by Kolokolnikov et al. [9, Section 5]. We note that the fold of the spots

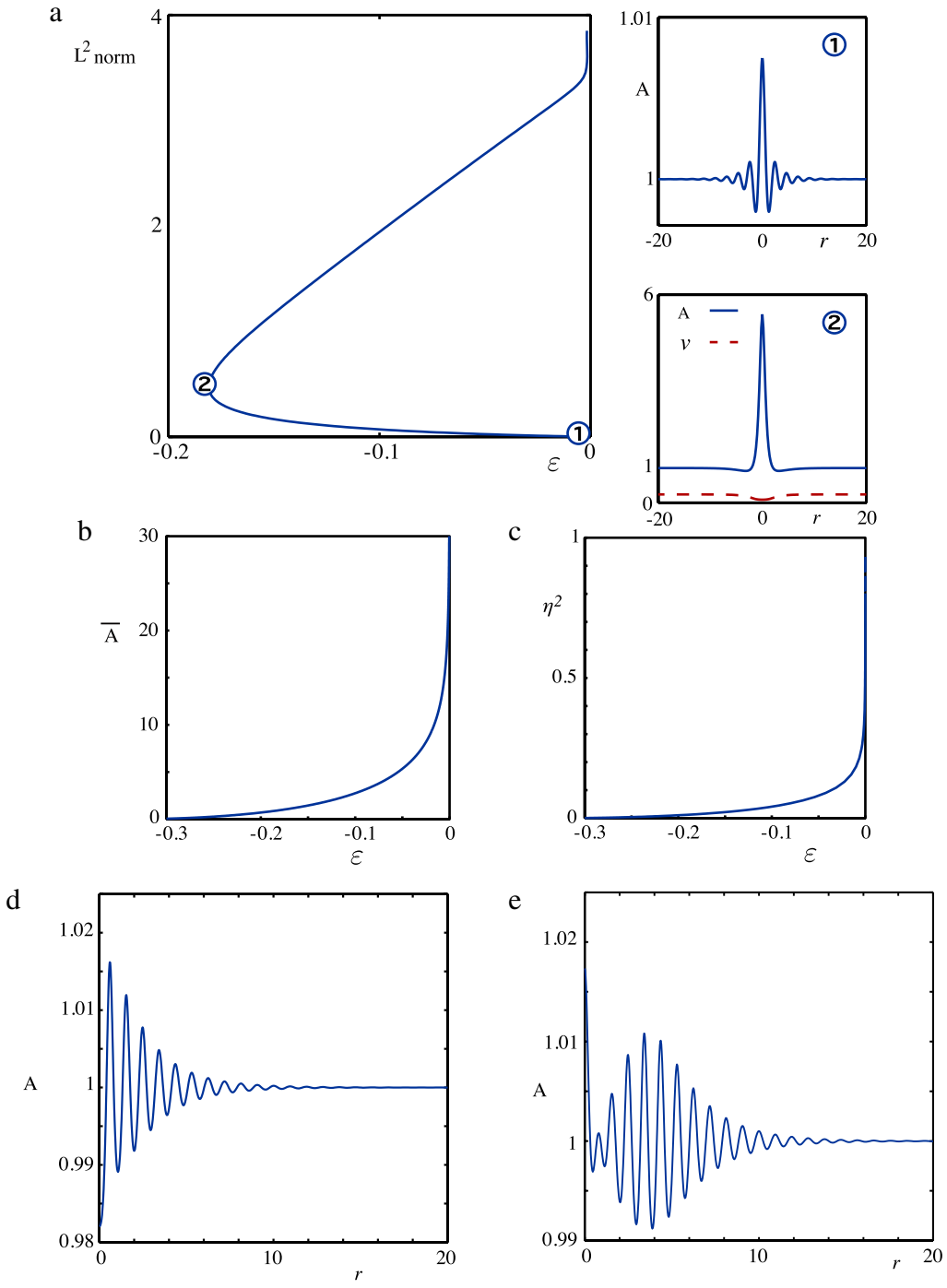


**Fig. 8.** (a) Radial localised spot bifurcation diagram for $\eta^2 = 0.015$, $\bar{A} = 1$, (b) and (c) two parameter continuation of the primary spot fold. In panel (d) we plot a Spot B and panel (e) a ring solution for $\eta^2 = 0.0005$, $\bar{A} = 1$, $\epsilon = -0.0001$.

in Fig. 8 converges to $\epsilon = -1/3$ as $\eta \to 0$ as predicted by the singular limit analysis. These spots are related to those found by Short et al. [7,8] except the spots we find are on the plane and decay exponentially while those found by Short only exist on discs of radius $R$ where $J_0(R) = 0$ and have $\mathcal{O}(1/\sqrt{R})$ decay to the spatially homogeneous state. Unlike in one-dimension, we do not observe any homoclinic snaking and numerics fail as the spot on the upper branch in Fig. 8(a) approaches the Turing point $\epsilon = 0$. In Fig. 8(d) and (e), we also plot a localised ring and Spot B. These states are found by using Matlab's `fsolve` Globalised Newton solver and providing an initial guess that is either a ring or spot B; see [18]. We do not observe the growth and interchange with the ring or Spot B solution found for the Swift–Hohenberg equation by McCalla & Sandstede [20].

### 5.2. Hexagon fronts

We employ the numerical methods described in Avitabile et al. [34], where we use a Fourier pseudo-spectral method in the periodic $y$ direction (for $\langle 10 \rangle$ fronts $y \in [0, 2\pi k^*_{crit}/\sqrt{3}]$ and for $\langle 11 \rangle$ fronts $y \in [0, 2\pi k^*_{crit}]$) and use AUTO07P [24] to solve the resulting first-order system in the unbounded $x$-direction. The solutions are computed on the positive quadrant with Neumann

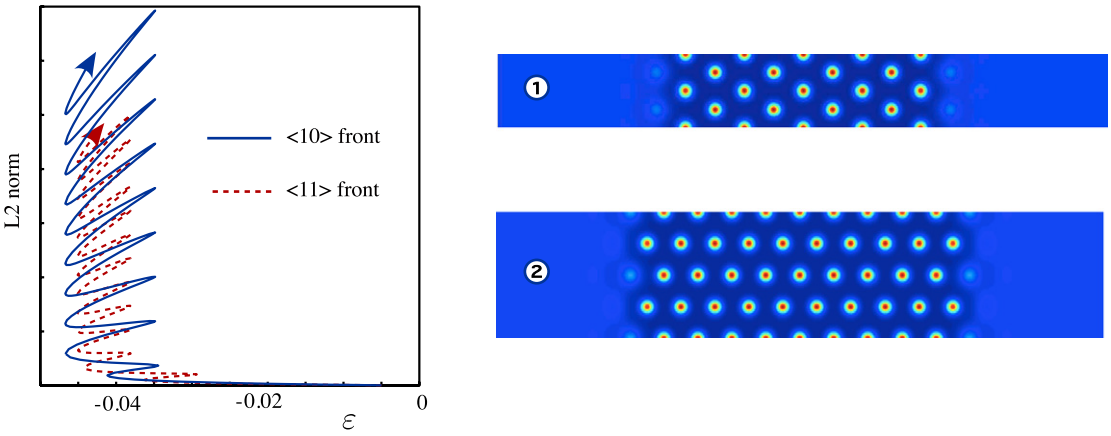


**Fig. 9.** Bifurcation diagram for both the ⟨10⟩- and ⟨11⟩-hexagon fronts with $\bar{A} = 1$, $\eta^2 = 0.1$.

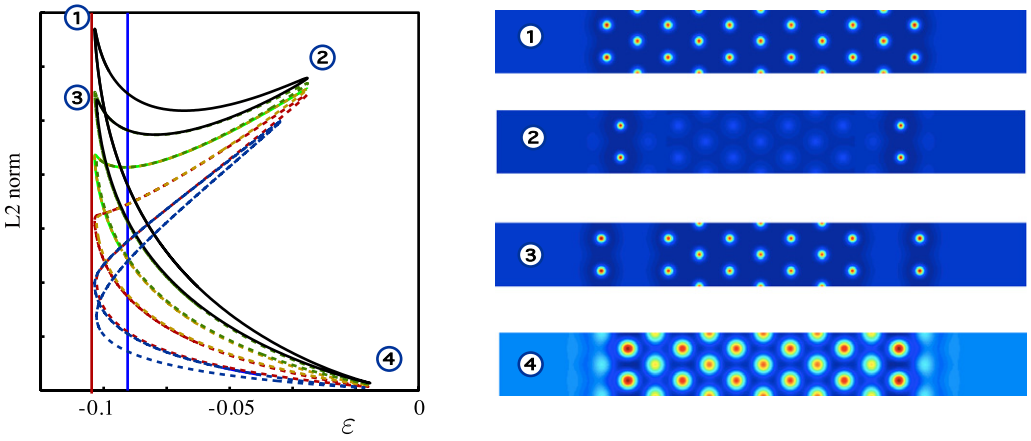


**Fig. 10.** Hexagon ⟨10⟩ front isolas with $\bar{A} = 1$, $\eta^2 = 0.04$. The labelled solutions are for the solid isola branch. The domain covering hexagon fold occurs at $\epsilon = -0.092$ while the radial spot fold occurs at $\epsilon = -0.103$ and lines up with the folds of the ⟨10⟩ fronts.

boundary conditions. Typical mesh sizes are NTST = 100 on $x \in [0, 100]$ and 20 collocation points in the $y$-direction.

To describe different directions and interfaces on the hexagon lattice we use the Bravais–Miller index notation; see [18]. On a hexagonal lattice there are two principal directions ⟨10⟩- and ⟨11⟩-directions, that are at $\pi/3$ radians apart.

Setting $\bar{A} = 1$, $\eta^2 = 0.1$, we show the bifurcation diagram for both the principal ⟨10⟩- and ⟨11⟩-hexagon fronts in Fig. 9. Here we observe the same type of snaking behaviour seen in the Swift–Hohenberg equation [18] where the ⟨10⟩-front (label (1) in Fig. 9) snakes over a larger region of parameter space than the ⟨10⟩-front (label (2) in Fig. 9). As one proceeds up the snake, entire rows of hexagon cells are added to both ends of the interface. We also expect there to be almost hexagon fronts where single cells are grown along the edge of the interface; see Lloyd et al. [18, Figure 21].

As we decrease $\eta$, we find that the bifurcation diagram is made up of isolas of hexagon fronts that go beyond the saddle–node point for the domain covering hexagons; see Fig. 10. These parameter values are the same as those used by Short et al. [7, Figure 7]. As one transverses the isolas, we see that the localised hexagon pattern passes to a multi-pulse state involving the hexagon cells; see panel (2) Fig. 10. In particular, we see that the left most folds of the ⟨10⟩-fronts occur at the fold of the radial spot strongly suggesting that the localised structure is made-up of radial spots. This explains why the fronts in Fig. 10 can exist beyond the fold of domain covering hexagons. However, it is clear that near the bottom right folds, the interior of the front does look like domain covering hexagons. We also note that decay to the background state changes from oscillatory to monotonic as one transverses the bifurcation diagram. This change in the type of decay to the background state is expected to have a significant effect on the multi-pulses observed as neither the theory of Knobloch & Wagenknecht [27] or Knobloch et al. [28], directly applies.

We show only a single isola for the ⟨11⟩-hexagon front in Fig. 11. As for the ⟨10⟩-front, we see that the hexagon cells become more localised and the left-most folds lining up with the fold of the spot. We also see that a multi-pulse states are created where the centre cells are missing. At the bottom right fold, the solution appears to be again made up again of hexagon cells rather than spots similar to that seen in Fig. 10 for the ⟨10⟩-front. The other ⟨11⟩-front isolas are more intricate but all the left-most folds line-up with the fold of the spot and we also see a variety of multi-pulses.

### 5.3. Hexagon patches

We numerically solve the (1.1) in polar coordinates $(r, \theta)$ and employ finite-differences in the radial direction and Fourier pseudo-spectral method in the angular direction. Neumann boundary conditions are applied at $r = 0$ where the discretised mesh is chosen to avoid a mesh point at the core. Furthermore, Neumann boundary conditions are applied in the angular direction and we compute on $\theta \in [0, \pi k^*_{crit}/3]$ to impose $\mathbb{D}_6$-symmetry. We use the EPCONT continuation algorithm described in [34].

We show the hexagon patch snaking bifurcation diagram starting from a radial spot for $\eta^2 = 0.1, \bar{A} = 1$ in Fig. 12. There is an initial $\mathbb{D}_6$-bifurcation off the radial spot where a branch develops into a hexagon patch by initially growing six hexagon cells to form a super-hexagon patch made up of six ⟨10⟩-hexagon

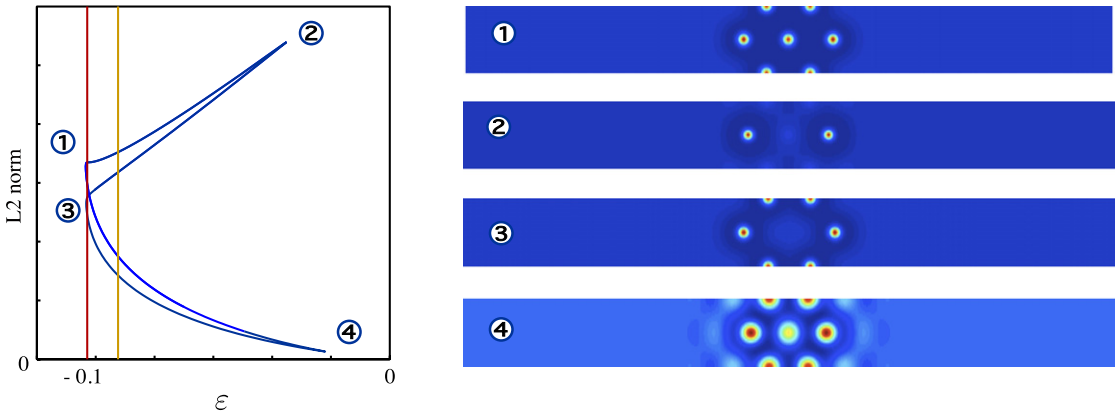


**Fig. 11.** Hexagon $\langle 11 \rangle$ front isola with $\bar{A} = 1$, $\eta^2 = 0.04$. The domain covering hexagon fold occurs at $\epsilon = -0.092$ while the radial spot fold occurs at $\epsilon = -0.103$ and lines up with the folds of the $\langle 11 \rangle$ fronts.

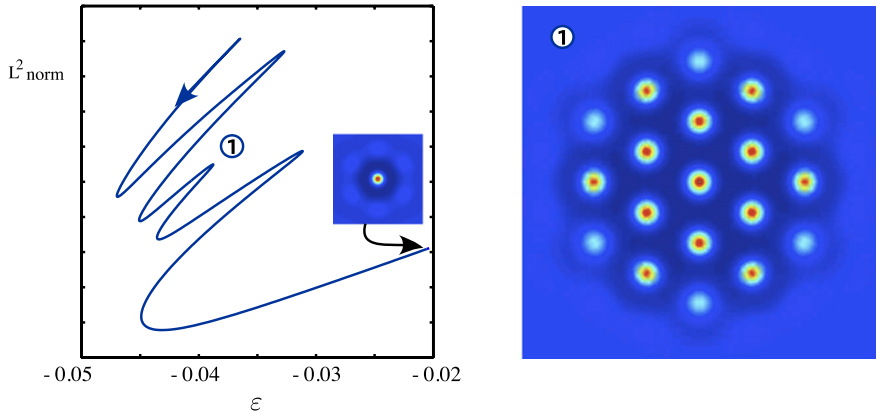


**Fig. 12.** Hexagon patch snaking bifurcation diagram for $\eta^2 = 0.1$, $\bar{A} = 1$. Here we see how a hexagon patch is grown from a $\mathbb{D}_6$-bifurcation off the radial spot. Six cells are initially grown until a super-hexagon patch (made up of $\langle 10 \rangle$-interfaces) is completed. Subsequent cells are grown from the centre and along the $\langle 10 \rangle$-interfaces.

interfaces. From there the next row of hexagon cells is added by first growing cells in the middle and along the six $\langle 10 \rangle$-interfaces to complete a new super-hexagon patch. This process is identical to that observed in the planar Swift–Hohenberg equation; see [18].

In Fig. 13(a), we show the bifurcation diagram starting from a seven cell hexagon patch with $\bar{A} = 1$, $\eta = 0.04$. We see that as one decreases $\epsilon$, the cells become more localised and start to resemble seven radial spots. As one proceeds around the fold labelled 3, the middle cell at the core decays to zero to create a ring of cells. This process is similar to that seen for the $\langle 11 \rangle$-front in Fig. 11. In Fig. 13(b), we compare the maximum height of the $A$-component of the system for both the patch and radial spot. Here we find excellent agreement suggesting the patch is made up of radial spots. This also explains why the patch exists in a parameter space that extends beyond the existence of domain covering hexagons.

## 6. Conclusion

In this paper, we have studied stationary, localised patterns bifurcating off the background state in the crime hotspot model (1.1) near the Turing instability and singular limit. The results in this paper show that the PDE system (1.1) possess a far richer set of solutions than just the domain covering periodic patterns analysed by Short et al. [7] and the spike solutions found in the $D \gg 1$ limit of (1.2) by Kolokolnikov et al. [9]. The main outcome of this paper is that both the singular limit and the Turing instability create stationary localised states that one can follow between these two regions in parameter space.

We find in one-dimension, homoclinic snaking for parameter values near the sub/supercritical Turing instability threshold away from the singular limit giving rise to infinitely many localised crime hotspots. Using numerics, we show that the localised patterns found in the homoclinic snaking region can pass to the singular limit $\eta \to 0$ where it appears that homoclinic snaking ceases and the localised solutions approach multi-pulse states. The singular limit analysis carried out in Section 4 shows that we expect to see homoclinic pulses connecting the spatially homogeneous steady state.

In two-dimensions, we find that spots bifurcate off the background state at the Turing instability for a larger range of parameter values than the one-dimensional pulses since the condition in Theorem 1 requires simply that $\theta \neq 0$ (i.e., up–down symmetry is broken at onset) rather than in 1D where we require that $\eta\sqrt{\bar{A}} \lesssim 0.157$. Away from the singular limit, the homoclinic snaking of hexagon fronts and patches is remarkably similar to that seen in the Swift–Hohenberg equation; see [18]. In particular that the $\langle 10 \rangle$-front snakes over a large region of parameter space than the $\langle 11 \rangle$-front and the snaking of $\mathbb{D}_6$-hexagon patches appears to be linked with the snaking of the fronts. This strongly suggests that there is a more fundamental mechanism relating the snaking of localised hexagon patterns for general non-variational systems. While we have not investigated the stability of the localised hexagon patterns, we anticipate that such solutions can be stable since the doubly-periodic hexagon patterns are stable in the same parameter region.

It is clear from the localised hexagon numerics that the singular limit has a dramatic effect on the homoclinic snaking structure. As one approaches the singular limit, the localised hexagon structures begin to act like a collection of multi-spots and the bifurcation

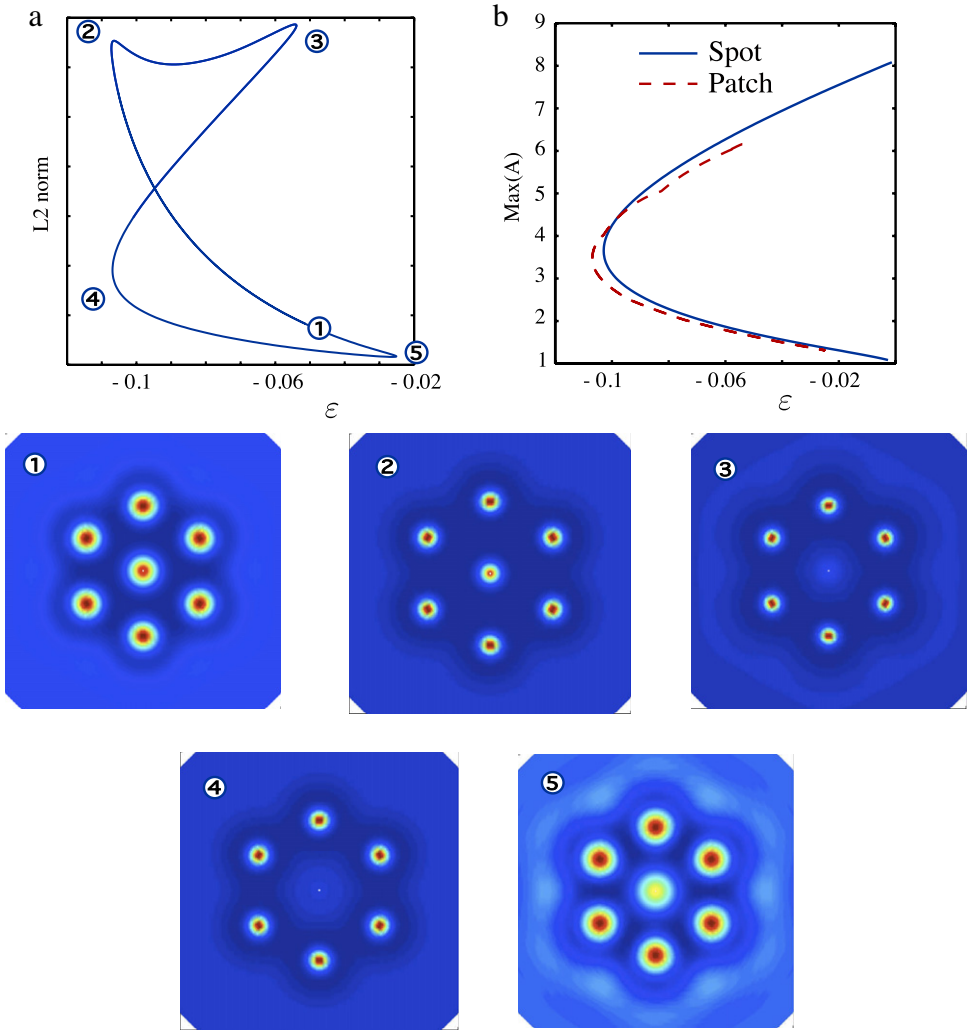


**Fig. 13.** (a) Hexagon patch bifurcation diagram for $\bar{A} = 1$, $\eta^2 = 0.04$, and (b) the maximum value of the radial spot (solid curve) and the patch (dashed curve).

diagram for both planar fronts and patches breaks up into isolas; see [35,36] for a singular limit analysis of localised hexagon structures in the Gierer & Meinhardt system. We believe near the singular limit, the one-dimensional localised patterns observed in the snaking region also approach a multi-pulse state and homoclinic snaking ceases. However, due to the difficultly in carrying out the analysis and numerics near the singular limit, it still may be possible that homoclinic snaking persists. We note that the singular limit in one-dimension appears to be geometrically similar to that in the Gray–Scott model (see [30]) albeit with a large excursion possible in the slow-manifold and we leave it as an open problem to rigorously prove the existence of the localised patterns found as $\eta \to 0$. It would also be interesting to see if homoclinic snaking is possible in the Gierer & Meinhardt system away from the singular limit. We note that similar one-dimensional snaking localised patterns (to those observed in Section 3) have also been observed in a neural-field model [37] where we believe that there is also a similar singular limit. Hence, we believe the type of homoclinic snaking (and geometry of the slow/fast manifolds) observed in Section 3, occurs in a range of different models beyond the one studied here.

We have left the analysis of the precise transition from homoclinic snaking to multi-pulse for further investigation. Furthermore, we have not investigated stability of the localised patterns found in this paper. However, we expect that some of these states studied in this paper are stable and there may be bifurcations to other localised states not explored in this paper. In Kolokolnikov [9], they found that there was Hopf bifurcation of the hotspots in a small region of parameter space but for most parameter values no Hopf bifurcation occurred. However, it may be possible that there is a Hopf/travelling wave bifurcation of the localised states found in this paper giving rise to time-dependent localised patterns that have not so far been observed in (1.1); such states have been studied in other reaction–diffusion systems [38–40]. Another interesting direction would be to explore travelling localised hotspots (see for example [30]) and the derivation of multi-pulse interaction equations (see for example [41]). It is expected that other models of urban crime (such as [5,6]) also possess localised states and it would be interesting to see if the localised patterns in the models have the similar behaviour.

Looking at the urban crime context of the model, $\eta$ corresponds to the neighbourhood effects and the rate of diffusion of the attractiveness field. Short et al. [4] investigated the case when $\eta$ is small (i.e., near the singular limit studied in this paper) for both an agent-based model and the PDE model (1.1) and found many solutions consisting of multiple hotspots. These interacting spots have more freedom and may more closely match crime data that is not spatially doubly periodic. The one-dimensional multi-pulses away from the singular limit in the snaking region will likely lie on isolas overlaying the snaking branches; see [28]. Close to the singular limit, the multi-pulses will exist for the parameter region where a single spike exists and hence explain the existence of large highly localised crime spikes surrounded

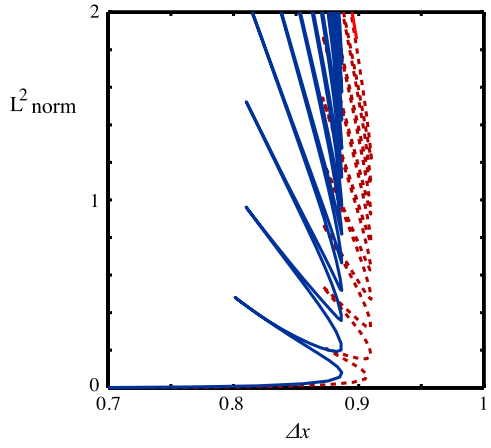


**Fig. 14.** Effect of increasing the 1D lattice distance on the localised patterns for $\bar{A} = 1$. Solid line $\eta^2 = 0.01$ and dashed line $\eta^2 = 0.015$.

by relative criminal quiescence. It would be desirable to derive a reduced set of equations for the interaction of pulses in the $\eta \to 0$ limit and we leave this as an open problem; see Sun et al. [42] and Doelman et al. [43] for a similar reduction for in the Gray–Scott and Gierer–Meinhardt models.

In this paper, we have concentrated on hotspots on the infinite-domain but the existence of hotspots on a finite domain is an interesting problem and important for understanding urban crime. On large finite-domains, the results in this paper are expected to persist (in particular, the numerical results in this paper are all computed on finite-domains). The effect of finite-domains on the homoclinic snaking scenario has been studied in a range of different models (see for instance [21,22]) where one initially observes homoclinic snaking before the branch connects to near the fold of the domain covering spatially periodic orbits. Near the singular limit on smaller finite-domains, one can construct periodic spikes using the same methods described in Section 4 (see for instance [44]) and new phenomena like peak insertion may appear [9].

We now discuss what might happen to these localised patterns in the agent-based model that the PDE system (1.1) was originally derived from. As the continuum limit is taken after averaging the stochastic based model, a first step towards understanding how the PDE solutions relate to the agent-based model is by simply applying second-order finite-difference scheme to the PDEs to investigate the effect of the lattice on the localised patterns. In Fig. 14, we show the effect of changing the lattice distance $\Delta x$ on the one-dimensional localised states. We see that as $\Delta x$ is increased, the localised patterns undergo homoclinic snaking similar to that seen by Yulin & Champneys [45] and Taylor & Dawes [46]. We also see that as $\eta$ is increased the localised patterns exist for a larger lattice distance but that there is a maximum lattice distance the localised states can exist for and that the width of the snaking region decreases. In the presence of noise, we expect these stationary localised patterns to become unstable (though they may be metastable for short time scales) and may either collapse, fill the domain with periodic pattern or begin travelling. We note that we have been unable to find (on time average) stationary localised structures in the same parameter region in the full stochastic agent-based model.

## Acknowledgements

HF gratefully acknowledges support from the UK Engineering and Physical Sciences Research Council Summer Bursary scheme. DL gratefully acknowledges partial support of the UK Engineering and Physical Sciences Research Council for programme grant EP/H021450/1 (Evolution and Resilience of Industrial Ecosystems (ERIE)) and the grant EP/H05040X/1 (Nucleation of Ferrosolitons and Localized Ferro-patterns). DL would like to thank Alan Champneys for first suggesting this problem, David Barton and Daniele Avitabile for useful discussions about the crime hotspot model and, Tasso Kaper and Björn Sandstede for insightful discussions about singular perturbation theory. The authors also thank Gianne Derks for comments on an earlier draft of the paper.

## Appendix. Radial normal form analysis

In this appendix we describe the modifications to the proof of the existence of Spot A in [19] required to prove Theorem 1.

We first re-write the time-independent radial PDE system (1.1) as a first-order ODE system to yield

$$A_r = B, \tag{A.1a}$$

$$B_r = -\frac{1}{r}B + \frac{A}{\eta^2} - \frac{A^0}{\eta^2} - \frac{\rho A}{\eta^2}, \tag{A.1b}$$

$$\rho_r = \sigma, \tag{A.1c}$$

$$\sigma_r = -\frac{1}{r}\sigma + 2\frac{\rho}{\eta^2 A}(A - A^0 - \rho A) + \frac{2}{A^2}(AB\sigma - \rho B^2) + \rho A + A^0 - \bar{A}. \tag{A.1d}$$

We now proceed to re-write this system as a Swift–Hohenberg equation. We solve the first two equations in (A.1) for $\rho$ and substitute these into the last two equations, setting $A = \bar{A} + B(r)$ and carrying out a Taylor series expansion about $B = 0$ we find

$$\eta^2\left(B_{rrrr} + \frac{B_r}{r^3} - \frac{B_{rr}}{r^2} + 2\frac{B_{rrr}}{r}\right) + \left(2 - \eta^2\bar{A} - 3\frac{A_0}{\bar{A}}\right)\left(B_{rr} + \frac{B_r}{r}\right) + \bar{A}B + B^2 - \eta^2\frac{B_rB}{r} - 4\frac{\eta^2 B_r B_{rrr}}{\bar{A}} + \frac{\eta^2}{\bar{A}}\frac{B_r^2}{r^2} - \eta^2 BB_{rr} - \frac{10\eta^2}{\bar{A}}\frac{B_rB_{rr}}{r} - \frac{2}{\bar{A}}B_r^2 + 6\frac{A_0}{\bar{A}^2}B_r^2 - \frac{3\eta^2}{\bar{A}}B_{rr}^2 + \frac{6A_0}{\bar{A}^2}B_r^2 - \frac{3\eta^2}{\bar{A}}B_{rr}^2 + \frac{3A_0}{\bar{A}^2}\frac{BB_r}{r} + \frac{3A_0}{\bar{A}}B_rB_{rr} + \mathcal{O}(B^3) = 0.$$

If we now employ the rescaling

$$B \to \frac{u}{\eta^2}, \qquad r \to r\eta\sqrt{\frac{2\bar{A}}{2\bar{A} - \eta^2\bar{A}^2 - 3A^0}},$$

we can re-write the equation as

$$(1 + \Delta_r)^2 u + \left(\frac{2\eta^2\bar{A}^3}{\left(2 - \eta^2\bar{A} - 3A_0\right)^2} - 1\right)u + f(u, u_r, u_{rr}, u_{rrr}) + \mathcal{O}(u^3) = 0, \tag{A.2}$$

where $f$ is a quadratic function given by

$$f(u, u_r, u_{rr}, u_{rrr}) = \frac{\alpha^4}{\eta^2}u^2 + \frac{\alpha^2}{\eta^2}\left(\frac{3A^0}{\bar{A}^2} - \eta\right)uu_r - \frac{8}{\bar{A}\eta}u_ru_{rrr} + \frac{1}{\bar{A}\eta}\frac{u_r^2}{r^2} + 2\frac{\alpha^2}{\eta^2\bar{A}}\left(\frac{6A^0}{\bar{A}} - 1\right)u_r^2 + \frac{\alpha}{\eta^2\bar{A}}(3A^0 - 10\eta)u_ru_{rr} - \frac{6}{\eta\bar{A}}u_{rr}^2 - \frac{\alpha^2}{\eta}uu_{rr},$$

where $\alpha = \eta\sqrt{\frac{2\bar{A}}{2\bar{A} - \eta^2\bar{A}^2 - 3A^0}}$.

Setting

$$\mu := \left(\frac{4\eta^2\bar{A}^3}{\left(2 - \eta^2\bar{A} - 3A_0\right)^2} - 1\right),$$

to be the bifurcation parameter, where a Turing instability occurs when $\mu = 0$ i.e., $A^0 = A^0_*$. We note that setting $A^0 = A^0_* + \epsilon$, $|\epsilon| \ll 1$, we find that $\mu = 3\epsilon/\eta\bar{A}^{3/2} + \mathcal{O}(\epsilon^2)$.

Expressing Eq. (A.2) as follows

$$\left(\partial_r^2 + \frac{1}{r}\partial_r + 1\right) u_1 = u_2,$$
$$\left(\partial_r^2 + \frac{1}{r}\partial_r + 1\right) u_2 = -\mu u_1 - f(u_1, (u_1)_r, (u_1)_{rr}, (u_1)_{rrr}) + \mathcal{O}(u_1^3),$$

we may re-write Eq. (A.2) as a four dimensional system of non-autonomous differential equations (see [19])

$$U_r = \mathcal{A}U + \mathcal{F}(U, \mu), \qquad \mathcal{A} = \begin{pmatrix} 0 & 0 & 1 & 0 \\ 0 & 0 & 0 & 1 \\ -1 & 1 & -\frac{1}{r} & 0 \\ 0 & -1 & 0 & -\frac{1}{r} \end{pmatrix}, \tag{A.3}$$

$$\mathcal{F} = \begin{pmatrix} 0 \\ 0 \\ 0 \\ \mathcal{F}_4(u_1, u_2, u_3, u_4, \mu) \end{pmatrix},$$

where $U = (u_1, u_2, u_3, u_4)^T$ and

$$\mathcal{F}_4(u_1, u_2, u_3, u_4, \mu) = -\mu u_1 - f\left(u_1, u_3, -u_1 + u_2 - \frac{1}{r}u_3, \frac{1}{r}u_1 - \frac{1}{r}u_2 + \left(\frac{2}{r^3} - 1\right)u_3 + u_4\right) + \mathcal{O}(u_1^3).$$

We note that the linear system $U_r = \mathcal{A}(r)U$ has four linearly independent solutions

$$V_1(r) = \sqrt{2\pi}(J_0(r), 0, -J_1(r), 0)^T,$$
$$V_2(r) = \sqrt{2\pi}(rJ_1(r), 2J_0(r), rJ_0(r), -2J_1(r))^T,$$
$$V_3(r) = \sqrt{2\pi}(Y_0(r), 0, -Y_1(r), 0)^T,$$
$$V_4(r) = \sqrt{2\pi}(rY_1(r), 2Y_0(r), rY_0(r), -2Y_1(r))^T.$$

Following Lloyd & Sandstede [19], in order to construct localised spots, one needs to show that there is a non-degenerate quadratic tangency of the centre unstable manifold from the core at $\mu = 0$. In particular, we need the following Lemma that is a slight modification of Lemma 1 in [19].

**Lemma 1.** *Fix $r_0 > 0$, then there are constants $\delta_0, \delta_1 > 0$ so that the set $W^{\mathrm{cu}}_-(\mu)$ of solutions $U(r)$ of (A.3) for which $\sup_{0\le r\le r_0}|U(r)| < \delta_0$ is, for $|\mu| < \delta_0$, a smooth two-dimensional manifold. Furthermore, $U \in W^{\mathrm{cu}}_-(\mu)$ with $|P^{\mathrm{cu}}_-(r_0)U(r_0)| < \delta_1$ if and only if*

$$\begin{aligned} U(r_0) = {} & d_1V_1(r_0) + d_2V_2(r_0) + V_3(r_0)\mathrm{O}_{r_0}(|\mu||d| + |d|^2) \\ & + V_4(r_0)\left([\theta_1 + \mathrm{o}(1)]d_1^2 + [\theta_2 + \mathrm{o}(1)]d_1d_2 \right. \\ & \left. + [\theta_3 + \mathrm{o}(1)]d_2^2 + \mathrm{O}_{r_0}(|\mu||d| + |d|^3)\right), \end{aligned} \tag{A.4}$$

*for some $d = (d_1, d_2) \in \mathbb{R}^2$ with $|d| < \delta_1$, where the right-hand side in (A.4) depends smoothly on $(d, \mu)$, $\mathrm{o}(1)$ is the Landau symbol in $r_0$ as $r_0 \to \infty$ and $\theta_1, \theta_2, \theta_3$ are constants depending on $\bar{A}, A^0_*$ and $\eta$. In particular,*

$$\begin{aligned} \frac{8\theta_1}{\sqrt{2\pi}} = {} & \frac{\alpha^4}{\eta^4}\frac{4}{\sqrt{3}} + \frac{\alpha^2}{\eta^4}\left(\frac{3A^0_*}{\bar{A}^2} - \eta^2\right)\left(-\frac{2}{\sqrt{3}}\right) \\ & - \frac{8}{\bar{A}\eta^2}\left(-\frac{2}{\sqrt{3}} - \frac{10\pi}{3} - \sqrt{3}\right) + \frac{1}{\bar{A}\eta^2}\left(\frac{8\pi}{3} + \sqrt{3}\right) \\ & + 2\frac{\alpha^2}{\eta^4\bar{A}}\left(\frac{6A^0_*}{\bar{A}} - 1\right)\frac{2}{\sqrt{3}} + \frac{\alpha}{\eta^4\bar{A}}(3A^0_* - 10\eta^2) \\ & \times \left(\frac{2}{\sqrt{3}} - 2\pi I_1\right) - \frac{6}{\eta^2\bar{A}}\left(\frac{4}{\sqrt{3}} + \frac{4\pi}{3} + \sqrt{3}\right) \\ & - \frac{\alpha^2}{\eta^2}\left(\frac{2\pi}{3} - \frac{4}{\sqrt{3}}\right), \end{aligned}$$

*where we evaluate $\theta_1$ at $\mu = 0$ (i.e. $A^0 = A^0_*$) and*

$$I_1 = \int_0^\infty J_0(r)J_1(r)^2 dr \sim 0.186.$$

The proof of Lemma 1 is the same as that in [19] except for the calculation of the quadratic coefficients $\theta_1, \theta_2, \theta_3$. For the exist of Spot A, we only need to calculate $\theta_1$ and find when it is non-zero. The $\theta_1$ coefficient is found by calculating the integral (the last integral in [19, Eq. 2.7])

$$\theta_1 = \frac{\sqrt{2\pi}}{8}\int_0^\infty rJ_0(r) f\left(\sqrt{2\pi}J_0(r), -\sqrt{2\pi}J_1(r), -\sqrt{2\pi}(J_0(r) - \frac{1}{r}J_1(r)), \sqrt{2\pi}(J_1(r) + \frac{1}{r}J_0(r) - \frac{2}{r^2}J_1(r))\right) dr.$$

To calculate the Bessel integrals, we use the following relations from Watson [47]

$$\int_0^\infty J_\nu(ar)J_\nu(br)J_\nu(cr)r^{1-\nu}dr = \frac{2^{\nu-1}\Delta^{2\nu-1}}{(abc)^\nu\Gamma(\nu + \frac{1}{2})\Gamma(\frac{1}{2})},$$
$$\int_0^\infty J_\mu(ar)J_\nu(br)J_\nu(cr)r^{1-\mu}dr = \frac{(bc)^{\mu-1}\sin(A)^{\mu-\frac{1}{2}}}{\sqrt{2\pi}a^\mu}P^{\frac{1}{2}-\mu}_{\nu-\frac{1}{2}}(\cos(A)),$$

where $\Delta$ is the area of the triangle of sides $a, b, c$ and $A = \arccos\left(\frac{b^2+c^2-a^2}{2bc}\right)$ and $P$ is the associated Legendre function. Almost all the Bessel integrals have explicit solutions except the integral $I_1$ which we have been unable to find an explicit solution for.

The matching of the core manifold

$$\begin{aligned} W^{cu}_-(\mu)|_{r=r_0} : \begin{pmatrix} A \\ B \end{pmatrix} = {} & \mathrm{e}^{\mathrm{i}[-\pi/4 + \mathrm{O}(1/r_0^2) + \mathrm{O}_{r_0}(|\mu| + |d|^2)]} \\ & \times \left(d_1[1 + \mathrm{O}(r_0^{-1})] - d_2[\mathrm{i} + \mathrm{O}(r_0^{-1})] + \mathrm{O}_{r_0}(|\mu||d| + |d|^2)\right. \\ & - d_2r_0^{-1}[\mathrm{i} + \mathrm{O}(r_0^{-1})] - [\theta_1 + \mathrm{o}(1)]\sqrt{r_0}d_1^2 - [\theta_2 + \mathrm{o}(1)] \\ & \times \frac{1}{\sqrt{r_0}}d_1d_2 - [\theta_3 + \mathrm{o}(1)]\frac{1}{r_0^{3/2}}d_2^2 \\ & \left. + \mathrm{O}_{r_0}(|\mu||d| + |d_2|^2 + |d_1|^3)\right), \end{aligned}$$

where $A, B$ are the normal form coordinates in [19, Lemma 2] and $(d_1, d_2) = (\tilde{d}_1/\sqrt{r_0}, \sqrt{r_0}\tilde{d}_2)$ with the far-field manifold [19, Eq. (5.10)]

$$W^s_+(\mu) : \begin{pmatrix} A \\ B \end{pmatrix} = \sqrt{\mu}\beta\begin{pmatrix} 1 \\ 0 \end{pmatrix} + \mu\beta\left[-\frac{1}{2} + \mathrm{O}(s_1) + \mathrm{O}_{s_1}(\mu + \sqrt{\mu}|\eta|^2)\right]\begin{pmatrix} r_0 \\ 1 \end{pmatrix} \tag{A.5}$$

now proceeds in exactly the same fashion as in [19, Section 5]. Re-defining $\beta$ to remove the phase in $W^{cu}_-(\mu)|_{r=r_0}$ and setting

$d_j = \sqrt{\mu}\hat{d}_j$ and writing $\beta = \beta_1 + i\beta_2$ one has to solve the matching equations

$$\begin{aligned}
&\hat{d}_1 - i\hat{d}_2 - i\beta_2 + \mathrm{O}(r_0^{-1})\hat{d} + \mathrm{O}_{r_0}(\mu|\hat{d}| + \sqrt{\mu}|\hat{d}|^2) \\
&\quad = \beta_1 + \sqrt{\mu} r_0 \mathrm{O}(\beta), \qquad \text{(A.6a)} \\
&-i\hat{d}_2 + \mathrm{O}(r_0^{-1})\hat{d}_2 - (\theta_1 + \mathrm{o}(1)) r_0^{3/2}\sqrt{\mu}\hat{d}_1^2 \\
&\qquad - (\theta_2 + \mathrm{o}(1))\sqrt{r_0}\sqrt{\mu}\hat{d}_1 d_2 - (\theta_3 + \mathrm{o}(1))\frac{1}{\sqrt{r_0}}\sqrt{\mu}\hat{d}_2^2 \\
&\qquad + \mathrm{O}_{r_0}(\mu|\hat{d}| + \mu|\hat{d}|^3) \\
&\quad = \sqrt{\mu} r_0 \beta \left[ -\frac{1}{2} + \mathrm{O}(s_1 + r_0^{-2}) + \mathrm{O}_{s1}(\sqrt{\mu}) \right]. \qquad \text{(A.6b)}
\end{aligned}$$

For $r_0 \gg 1$ sufficiently large but fixed, we can solve the $(\Re A, \Im A, \Im B)$-components of this equation for $(\tilde{d}_1, \tilde{d}_2, \beta_2)$ as a function of $(\beta_1, \mu)$, and we have the expansion

$$\tilde{d}_1 = \beta_1 + \mathrm{O}(\sqrt{\mu}\beta_1), \qquad \tilde{d}_2 = \mathrm{O}(\sqrt{\mu}\beta_1),$$
$$\beta_2 = \mathrm{O}(1/r_0)\beta_1 + \mathrm{O}(\sqrt{\mu}\beta_1).$$

Substituting this solution into (A.6) and projecting it onto the remaining $(\Re B)$-component along the range of the linear map $\tilde{d}_2 \mapsto (-\mathrm{i} + \mathrm{O}(1/r_0))\tilde{d}_2$, we arrive at the equation

$$\begin{aligned}
&-[\theta_1 + \mathrm{o}(1)]\, r_0^{\frac{3}{2}} \beta_1^2 + \mathrm{O}_{r_0}(\mu\beta_1) \\
&\quad = r_0 \beta_1 \left[ -\frac{1}{2} + \mathrm{O}(1/r_0) + \mathrm{O}(s_1) + \mathrm{O}_{s_1}(\sqrt{\mu}) \right].
\end{aligned}$$

Factoring out the trivial solution $\beta_1 = 0$, which corresponds to $u = 0$, we solve the equation

$$\begin{aligned}
&-[\theta_1 + \mathrm{o}(1)]\sqrt{r_0}\nu\beta_1 + \mathrm{O}_{r_0}(\mu) \\
&\quad = -\frac{1}{2} + \mathrm{O}(1/r_0) + \mathrm{O}(s_1) + \mathrm{O}_{s_1}(\sqrt{\mu}),
\end{aligned}$$

which has the unique small solution

$$\beta_1 = \frac{1 + \mathrm{O}(1/r_0) + \mathrm{O}(s_1) + \mathrm{O}_{s_1}(\sqrt{\mu})}{2\sqrt{r_0}\theta_1} \neq 0.$$

In particular, transforming back to the original amplitudes $d_1$ and $d_2$, and reversing $(d_1, d_2) = (\tilde{d}_1/\sqrt{r_0}, \sqrt{r_0}\tilde{d}_2)$, we see that

$$d_1 = \frac{\sqrt{\mu}}{2\theta_1} \neq 0, \qquad d_2 = \mathrm{O}(\mu)$$

as claimed.

## References


[1] P.J. Brantingham, P.L. Brantingham, Patterns in Crime, Macmillan, New York, 1984.
[2] S.D. Johnson, K. Bowers, New insights into the spatial and temporal distribution of repeat victimization, British J. Crimi. 37 (1997) 224–241.
[3] J.Q. Wilson, G.L. Kelling, Broken windows and police and neighborhood safety, Atl. Monthly 249 (1982) 29–32.
[4] M. Short, M. D'Orsogna, A statistical model of criminal behavior, Math. Models Methods Appl. Sci. 18 (2008) 1249–1267.
[5] A.B. Pitcher, Adding police to a mathematical model of burglary, European J. Appl. Math. (2010) 1–19.
[6] H. Berestycki, J.-P. Nadal, Self-organised critical hot spots of criminal activity, European J. Appl. Math. 21 (2010) 371–399.
[7] M.B. Short, A.L. Bertozzi, Nonlinear patterns in urban crime: hotspots, bifurcations, and suppression, SIAM J. Appl. Dyn. Syst. Vol. 9 (No. 2) (2010) 462–483.
[8] M.B. Short, P.J. Brantingham, A.L. Bertozzi, G.E. Tita, Dissipation and displacement of hotspots in reaction–diffusion models of crime, PNAS 107 (2010) 3961–3965.
[9] T. Kolokolnikov, M.J. Ward, J. Wei, The stability of steady-state hot-spot patterns for a reaction–diffusion model of urban crime, DCDS-B 2012 (in press).
[10] J. Swift, P.C. Hohenberg, Hydrodynamic fluctuations at the convective instability, Phys. Rev. A 15 (1977) 319–328.
[11] P.D. Woods, A.R. Champneys, Heteroclinic tangles and homoclinic snaking in the unfolding of a degenerate reversible Hamiltonian–Hopf bifurcation, Physica D 129 (1999) 147–170.
[12] J. Burke, E. Knobloch, Normal form for spatial dynamics in the Swift–Hohenberg equation, Discrete Contin. Dyn. Syst. (2007) 170–180.
[13] S.J. Chapman, G. Kozyreff, Exponential asymptotics of localized patterns and snaking bifurcation diagrams, Physica D 238 (2009) 319–354.
[14] J.H.P. Dawes, The emergence of a coherent structure for coherent structures: localized states in nonlinear systems, Philos. Trans. R. Soc. Lond. Ser. A Math. Phys. Eng. Sci. 368 (2010) 3519–3534.
[15] E. Knobloch, Spatially localized structures in dissipative systems: open problems, Nonlinearity 21 (2008) T45–T60.
[16] P. Coullet, C. Riera, C. Tresser, Stable static localized structures in one dimension, Phys. Rev. Lett. 84 (2000) 3069–3072.
[17] J. Burke, E. Knobloch, Homoclinic snaking: structure and stability, Chaos 17 (2007) 037102. 15.
[18] D.J.B. Lloyd, B. Sandstede, D. Avitabile, A.R. Champneys, Localized hexagon patterns of the planar Swift–Hohenberg equation, SIAM J. Appl. Dynam. Syst. 7 (2008) 1049–1100.
[19] D.J.B. Lloyd, B. Sandstede, Localized radial solutions in the Swift–Hohenberg equation, Nonlinearity 22 (2009) 485–524.
[20] S. McCalla, B. Sandstede, Snaking of radial solutions of the multi-dimensional Swift–Hohenberg equation: a numerical study, Physica D 239 (2010) 1581–1592.
[21] J.H.P. Dawes, Modulated and localized states in a finite domain, SIAM J. Appl. Dyn. Syst. 8 (2009) 909–930.
[22] D. Lo Jacono, A. Bergeon, E. Knobloch, Spatially localized magnetoconvection, Fluid Dyn. Res. 44 (2012) 031411. 12.
[23] C.J. Budd, R. Kuske, Localized periodic patterns for the non-symmetric generalized Swift–Hohenberg equation, Physica D 208 (2005) 73–95.
[24] E.J. Doedel, B. Oldeman, AUTO07P: continuation and bifurcation software for ordinary differential equations, Technical Report, Concordia University, 2009.
[25] J. Burke, E. Knobloch, Localized states in the generalized Swift–Hohenberg equation, Phys. Rev. E 73 (2006) 056211.
[26] M. Beck, J. Knobloch, D. Lloyd, B. Sandstede, T. Wagenknecht, Snakes, ladders, and isolas of localised patterns, SIAM J. Math. Anal. 41 (2009) 936–972.
[27] J. Knobloch, T. Wagenknecht, Snaking of multiple homoclinic orbits in reversible systems, SIAM J. Appl. Dyn. Syst. 7 (2008) 1397–1420.
[28] J. Knobloch, D.J.B. Lloyd, B. Sandstede, T. Wagenknecht, Isolas of 2-pulse solutions in homoclinic snaking scenarios, J. Dynam. Differential Equations 23 (2011) 93–114.
[29] A.J. Homburg, B. Sandstede, in: H. Broer, F. Takens, B. Hasselblatt (Eds.), Handbook of Dynamical Systems III, Elsevier, 2010, pp. 379–524.
[30] A. Doelman, T.J. Kaper, P.A. Zegeling, Pattern formation in the one-dimensional Gray–Scott model, Nonlinearity 10 (1997) 523–563.
[31] N. Fenichel, Geometric singular perturbation theory for ordinary differential equations, J. Differential Equations 31 (1979) 53–98.
[32] S. McCalla, Localized structures in the multi-dimensional Swift–Hohenberg equation, Ph.D. Thesis, Brown University, 2011.
[33] A. Scheel, Radially symmetric patterns of reaction–diffusion systems, Mem. Amer. Math. Soc. 165 (2003) viii+86.
[34] D. Avitabile, D.J.B. Lloyd, J. Burke, E. Knobloch, B. Sandstede, To snake or not to snake in the planar Swift–Hohenberg equation, SIAM J. Appl. Dyn. Syst. 9 (2010) 704–733.
[35] M. del Pino, M. Kowalczyk, X. Chen, The Gierer & Meinhardt system: the breaking of homoclinics and multi-bump ground states, Commun. Contemp. Math. 3 (2001) 419–439.
[36] M. Del Pino, M. Kowalczyk, J. Wei, Multi-bump ground states of the Gierer–Meinhardt system in $\mathbb{R}^2$, Ann. Inst. H. Poincaré Anal. Non Linéaire 20 (2003) 53–85.
[37] G. Faye, J. Rankin, P. Chossat, Localized states in an unbounded neural field equation with smooth firing rate function: a multi-parameter analysis, J. Math. Bio. (2012).
[38] P. van Heijster, B. Sandstede, Planar radial spots in a three-component FitzHugh–Nagumo system, J. Nonlinear Sci. 21 (2011) 705–745.
[39] D. Avitabile, D.J.B. Lloyd, K. Ninsuman, B. Sandstede, D.Y. Yoon, Radial oscillons in two reaction–diffusion models (2013) (in preparation).
[40] J. Burke, J.H.P. Dawes, Localized states in an extended Swift–Hohenberg equation, SIAM J. Appl. Dyn. Syst. 11 (1) (2012) 261–284.
[41] S. Zelik, A. Mielke, Multi-pulse evolution and space–time chaos in dissipative systems, Mem. Amer. Math. Soc. 198 (2009) vi+97.
[42] W. Sun, M.J. Ward, R. Russell, The slow dynamics of two-spike solutions for the Gray–Scott and Gierer–Meinhardt systems: competition and oscillatory instabilities, SIAM J. Appl. Dyn. Syst. 4 (2005) 904–953 (electronic).
[43] A. Doelman, T.J. Kaper, Semistrong pulse interactions in a class of coupled reaction–diffusion equations, SIAM J. Appl. Dyn. Syst. 2 (2003) 53–96 (electronic).
[44] D.S. Morgan, A. Doelman, T.J. Kaper, Stationary periodic patterns in the 1D Gray–Scott model, Methods Appl. Anal. 7 (2000) 105–149.
[45] A.V. Yulin, A.R. Champneys, Discrete snaking: multiple cavity solitons in saturable media, SIAM J. Appl. Dyn. Syst. 9 (2010) 391–431.
[46] C. Taylor, J.H.P. Dawes, Snaking and isolas of localised states in bistable discrete lattices, Phys. Lett. A 375 (2010) 14–22.
[47] G.N. Watson, A treatise on the theory of Bessel functions, in: Cambridge Mathematical Library, Cambridge University Press, Cambridge, 1995. Reprint of the second (1944) edition.